THE GEOLOGICAL SOCIETY OF AMERICA®

Microstructural constraints on magma emplacement and sulfide transport mechanisms

Z. Vukmanovic[1,*], M.L. Fiorentini[2], S.M. Reddy[3], and B. Godel[4]

[1]DEPARTMENT OF EARTH SCIENCES, UNIVERSITY OF CAMBRIDGE, CAMBRIDGE CB2 3EQ, UK
[2]CENTRE FOR EXPLORATION TARGETING AND ARC CENTRE OF EXCELLENCE FOR CORE TO CRUST FLUID SYSTEMS, SCHOOL OF EARTH SCIENCES, THE UNIVERSITY OF WESTERN AUSTRALIA, PERTH, WESTERN AUSTRALIA 6009, AUSTRALIA
[3]SCHOOL OF EARTH AND PLANETARY SCIENCES, CURTIN UNIVERSITY, GPO BOX U1987, PERTH, WESTERN AUSTRALIA 6845, AUSTRALIA
[4]COMMONWEALTH SCIENTIFIC AND INDUSTRIAL RESEARCH ORGANISATION (CSIRO) MINERAL RESOURCES, AUSTRALIAN RESOURCE RESEARCH CENTER–PERTH, KENSINGTON, WESTERN AUSTRALIA 6151, AUSTRALIA

ABSTRACT

The poorly constrained nature of the physical transfer of sulfides along magmatic conduits has implications for the genesis and localization of mineral deposits as well as for understanding the large-scale mobility of volatiles and metals across different geochemical reservoirs. Our natural laboratory to address this topic is a sulfide-bearing ultramafic pipe emplaced in the deep crust of the Ivrea-Verbano Zone, northwest Italy. The pipe is composed of volatile-rich peridotite that contains disseminated, blebby, and semimassive sulfides enriched in nickel, copper, and platinum-group elements (PGEs). The integration of electron backscatter diffraction orientation data and three-dimensional (3-D) X-ray computed tomography analyses from this study indicated that (1) most of olivine crystallized upon emplacement of the magma; (2) the shape and texture of the intragranular sulfide blebs, principally hosted within the central portions of the pipe, reflect early sulfide saturation; and (3) marginal areas record higher strain compared to the cores of the pipes. The differences in the size distribution of the sulfide grains between the central and marginal areas of the pipe are due to magma emplacement dynamics. The larger sulfide aggregates forming the bulk of the Ni-Cu-PGE sulfide mineralization along the margins of the pipe are interpreted to have formed by coalescence of a large number of smaller sulfide droplets. The observed sulfide size distribution between the central and marginal areas of the Valmaggia pipe is principally due to the dynamics of the magma upon emplacement, and it locally records the role of water- and carbon dioxide–bearing volatiles in the physical entrainment of dense sulfide liquids. These processes provide a viable mechanism to transport sulfides enriched in chalcophile and siderophile metals from the upper mantle into the lower continental crust, where they may be available for later remobilization into ore systems that may form subsequently in the middle and upper crust.

LITHOSPHERE GSA Data Repository Item 2018417 https://doi.org/10.1130/L743.1

INTRODUCTION

The Ivrea-Verbano Zone (IVZ) in northwest Italy is composed of (1) mantle-derived mafic magmas (the mafic complex) that intruded the metamorphic continental basement of the southern Alps (the Kinzigite Formation), and (2) large fragments of mantle peridotites that outcrop along the Insubric Line (Fig. 1; Peressini et al., 2007; Quick et al., 1994). These peridotites are interpreted to represent sections of the lithospheric mantle (Garuti et al., 1980; Mehnert, 1975; Rutter et al., 1993) that were exhumed during three discrete tectonic phases, starting in the Jurassic Period until the late Miocene Epoch (Wolff et al., 2012).

Despite the wealth of previous work in the region, limited research has been undertaken on a series of Permian–Triassic ultramafic alkaline pipes that intrude the upper part of the mafic complex and the lower portion of the Kinzigite Formation (Fiorentini et al., 2007, 2002, 2018; Garuti et al., 2001; Locmelis et al., 2016; Sessa et al., 2017; Zaccarini et al., 2014). These small intrusions (<300 m in diameter) consist of amphibole-rich peridotites with minor segregations of gabbroic composition. The pipes host disseminated, blebby, and semimassive magmatic sulfide mineralization, which is preferentially (but not solely) concentrated along their margins (Garuti et al., 2001). The pipes have been interpreted to represent the cumulate-rich intrusive remnants from the emplacement of the mafic magmas, which were derived from a previously depleted peridotite source that had been metasomatically enriched in alkalis, Cu, S, and platinum-group elements (PGEs; Fiorentini and Beresford, 2008; Garuti et al., 2001). More recently, Locmelis et al. (2016) put forward the hypothesis that the pipes were derived from melting of metasomatized lithospheric mantle pods that formed during Variscan subduction processes.

This study focused on unravelling the emplacement dynamics of the best-preserved and accessible of the five pipes that are currently known, the Valmaggia pipe (Fig. 1). The rocks forming the pipe and its sulfide mineralization are interpreted to be cumulates that crystallized under lower-crustal conditions (≤0.8 GPa) within feeder conduits for ascending basaltic magmas (Locmelis et al., 2016). The original cumulates were dunitic, but during cooling of the magmatic system, these reacted with hydrous melts (at 1000–1050 °C) to produce abundant amphibole and (to a lesser extent) orthopyroxene, together with residual olivine (Locmelis

Zoja Vukmanovic http://orcid.org/0000-0001-7559-0023
*zv211@cam.ac.uk

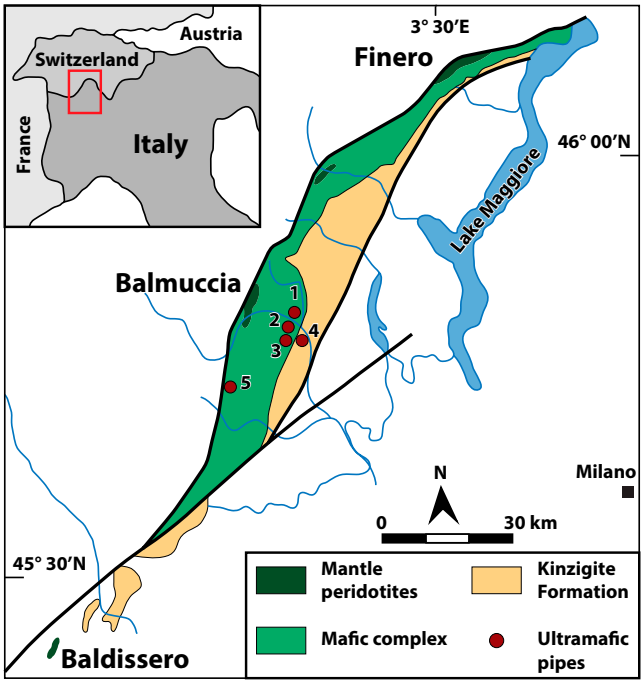

Figure 1. Geological map of Ivrea Verbano, modified after Quick et al. (2002). Location of the Valmaggia samples (red circles 1–4): 45°49′51.63″N, 8°13′25.07″E.

et al., 2016). The crystallization of plagioclase, phlogopite, spinel, minor apatite, and carbonate either occurred during this stage and/or during the final solidification of the trapped liquid.

The two samples selected for this study are representative of the internal and marginal areas of the pipe. Their choice from a large sample set collected over multiple field campaigns was based on their petrography, whole-rock geochemistry, and stable and radiogenic isotopic signatures (n > 50; Fiorentini et al., 2002, 2007, 2018; Locmelis et al., 2016; Sessa et al., 2017). The sampling sites were also carefully selected using a series of mining galleries excavated in the 1800s that crosscut the magmatic body. These galleries permitted the three-dimensional (3-D) characterization of the pipe geometry in relation to the country rocks (Sessa et al., 2017). With this integrated approach, the new combined electron backscatter diffraction (EBSD) and high-resolution X-ray computed tomography (HRXCT) data provide a unique opportunity to investigate in detail the mechanisms of emplacement and sulfide transport in deep magmatic systems.

The timing of the formation of the Ni-Cu-PGE sulfide mineralization associated with the pipes remains unclear. Two hypotheses exist: The first suggests that magmatic mineralization may have formed early, coeval with the initial stages of pipe emplacement. The second speculates that sulfides may have segregated in the pipe conduits during the emplacement of the hydrous melts that percolated through the cumulate pile during the final stages of crystallization. Our results indicate that these two end-member processes may not be mutually exclusive, with different magmatic sulfides forming at different stages during the complex emplacement history of the host pipe.

GEOLOGICAL BACKGROUND

Ivrea-Verbano Zone

The IVZ is a largely ellipsoidal body, ~150 km × 15 km, characterized by subvertical foliation, extending from northwest Italy into southern Switzerland (Fig. 1). To the west and northwest, the Canavese segment of the Insubric Line separates the IVZ from the Austroalpine Domain (Schmid et al., 1987). To the south and southeast, the Cremosina, Cossato-Mergozzo-Brissago, and Pogallo Lines separate the IVZ from the Strona-Ceneri Zone (Boriani et al., 1990).

The IVZ consists of three main lithological formations: (1) the mafic complex, (2) the mantle peridotites, and (3) the Kinzigite Formation (Fig. 1). The mafic complex can be subdivided into three units: the layered series (or Cyclic units), the main gabbro, and the diorite unit (e.g., Rivalenti et al., 1984; Pin and Sills, 1986; Quick et al., 1994; Garuti et al., 2001). The layered series is the lowermost unit and consists of a sequence of mafic-ultramafic layers intercalated with rafts of strongly migmatized metasedimentary rocks (Rivalenti et al., 1984; Garuti et al., 2001). It is overlain by the main gabbro, which grades upward into the diorite unit. A metasedimentary sequence up to 100 m thick separates the layered series and the main gabbro, suggesting that the two formations represent two different intrusive events (Ferrario et al., 1982; Garuti et al., 2001).

The top of the diorite unit intrudes the structurally higher Kinzigite Formation, which consists of a metamorphic sequence of middle-amphibolite- to granulite-facies rocks, primarily consisting of metapelites intercalated with mafic meta-igneous rocks, marbles, quartzites, and pegmatites (Bea and Montero, 1999; Schnetger, 1994; Guergouz et al., 2018). Finally, the mantle peridotites outcrop as few-kilometer-size massifs within the mafic complex. They are considered to represent obducted slices of the subcontinental mantle, which outcrop along the Insubric Line near Baldissero, Balmuccia, and Finero (Fig. 1; Shervais and Mukasa, 1991; Hartmann and Wedepohl, 1993).

Geometry and Composition of the Valmaggia Pipe

The Valmaggia pipe is the most accessible of the known pipes in the IVZ. Sessa et al. (2017) mapped this pipe in detail and produced a 3-D model, which shows the presence of a roughly ellipsoidal main body up to 300 m in diameter (Fiorentini et al., 2002; Garuti et al., 2001) elongated along NNE-SSW, dipping steeply (70°–90°) toward the WNW. The pipe includes three apophyses or branches. The complex geometry of these types of tubular bodies is widely presented in the literature, as summarized in Barnes et al. (2016).

The pipe rocks appear dark gray, with either a medium- or coarse-grained equigranular texture (Fig. 2), and they do not display any distinct layering. Furthermore, they have sharp contacts with the country rocks, without the development of any chilled margins, as shown in figure 2 of Locmelis et al. (2016). Conversely, there is a discontinuous but ubiquitous presence of 1–100-cm-thick pegmatoidal gabbroic pods along the margins (Locmelis et al., 2016; Sessa et al., 2017). In general, field relationships together with the occurrence of mafic-ultramafic lithologies, the ubiquitous presence of meso- to adcumulate textures, and the well-preserved magmatic geochemical signature are indicative of an intrusive igneous origin for the pipes (Garuti et al., 2001; Locmelis et al., 2016).

As for the time of emplacement, two main working hypotheses are currently laid out in the literature. Garuti et al. (2001) suggested that all pipes in the IVZ were emplaced synchronously ca. 290 Ma, broadly contemporaneous with the emplacement of the mafic complex at 288 ± 4 Ma (Peressini et al., 2007). According to Garuti et al. (2001), this suggests an intimate petrogenetic relationship between the crustal underplating event and the emplacement of the pipes. However, on the basis of high-precision isotope dilution–thermal ionization mass spectrometry (ID-TIMS) geochronology, Locmelis et al. (2016) and Fiorentini et al. (2018) put forward an alternative scenario: The alkaline pipes and their associated Ni-Cu-PGE sulfide mineralization were not emplaced synchronously, but over

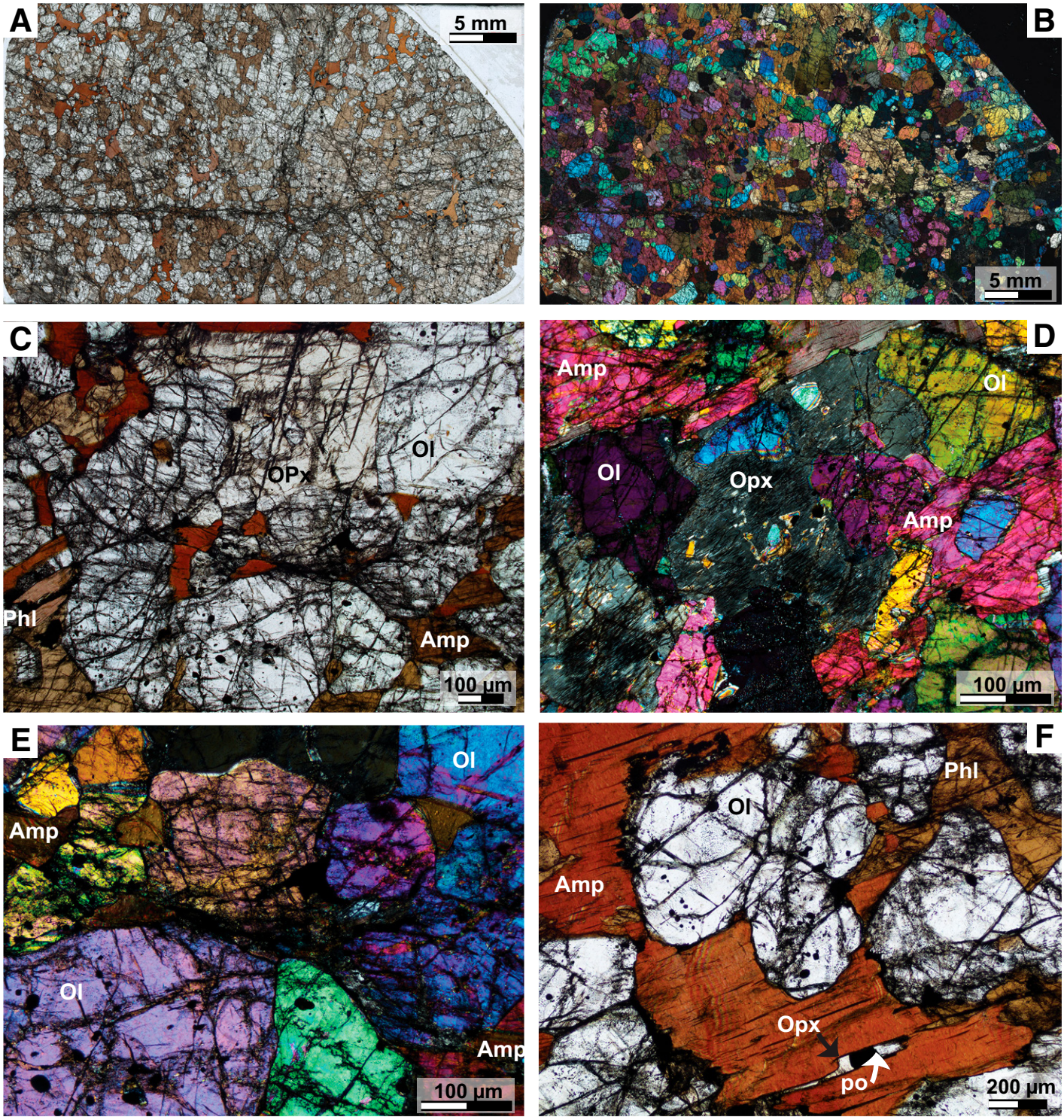

Figure 2. Photomicrographs of I2 (center of the pipe) Ivrea Verbano sample. (A) Plane-polarized photomicrograph of the entire thin section. (B) Cross-polarized photomicrograph of the entire thin section. (C) Olivine crystals are enclosed by oikocrysts, composed of amphibole and phlogopite. (D) Oikocryst of altered orthopyroxene surrounding olivine crystals. (E) Fractured olivine crystals with recrystallization zone at the contact between olivine grains. (F) Oikocrystic amphibole contains orthopyroxene and pyrrhotite along the cleavage plane. Abbreviations: Ol—olivine; Amp—amphibole; OPx—orthopyroxene; Phl—phlogopite; po—pyrrhotite.

a protracted time span of ~40 m.y. between ca. 290 Ma and ca. 250 Ma. Accordingly, the pipes would not have an intimate petrogenetic relationship with the voluminous intrusion of mantle-derived mafic magmas (the mafic complex) that underplated the metamorphic continental basement of the southern Alps (the Kinzigite Formation).

Magmatic Sulfide Mineralization

In the IVZ, magmatic sulfide occurrences are associated with sills, dikes, and pipes emplaced at various structural levels. Ni-Cu-PGE sulfide mineralization varies in texture, composition, grade, and tenor (Garuti et al., 1986). Low-grade sulfide mineralization is associated with peridotitic, pyroxenitic, and gabbroic dikes and sills that are intercalated with granulitic metasediments. These dikes and sills occur at the exhumed transition between mantle and crustal rocks, generally in the layered series or lowermost part of the main gabbro in the mafic complex. Higher-grade sulfide mineralization is associated with the five pipes intruding into the lower Kinzigite Formation (Fei di Doccio) and into the upper part of the main gabbro (Bec d'Ovaga, Castello di Gavala, Valmaggia, and Piancone la Frera), as shown in Figure 1.

The sulfide assemblage of the magmatic mineralization associated with the pipes consists mostly of pyrrhotite, pentlandite, and chalcopyrite, with minor amounts of cubanite, mackinawite, and pyrite, as well as PGE minerals (Zaccarini et al., 2014). The sulfides occur mainly along the outer rims of the pipes, predominantly as polyphase aggregates ranging in size between <0.01 mm and several millimeters in diameter. Sulfides are less abundant in the core of the pipes than in the outer rims. In the core of the pipes, they form polyphase pyrrhotite ± pentlandite blebs, with grain sizes between 100 and 1000 µm. According to Garuti et al. (2001) and Zaccarini et al. (2014), the sulfides texturally appear to have segregated as droplets from an immiscible sulfide liquid. The occurrence of sulfide veins crosscutting the rock suggests that some sulfides were remobilized and redeposited during postmagmatic processes.

METHODOLOGY

Samples I2 and I7 were collected from the core and the margin of the Valmaggia pipe, respectively. Specifically, sample I7 was collected ~1 m away from the sharp contact with the gabbro country rock. Both samples have been analyzed using standard petrographic techniques combined with EBSD, HRXCT, two-dimensional (2-D) and 3-D image analysis, and quantification. The orientation of the samples presented in this contribution is referenced to the arbitrary *x*-*y*-*z* coordinates of the random cuts through the sample and not to the larger-scale orientation of the pipe.

High-Resolution X-Ray Computed Tomography

After being mounted on the sample holder, each sample was scanned using the XRADIA (now Zeiss) VersaXRM500 3-D X-ray microscope installed at the Australian Resource Research Center (CSIRO, Perth, Western Australia) to determine the 3-D distribution, size, and morphology of the sulfide aggregates observed within each individual sample. For each sample, 1600 projections were recorded over 360° (i.e., 0.225 degree step between projections). Artifacts such as rings, beam hardening, and shifts were either minimized during the acquisition or corrected during the reconstruction. All projections were used to reconstruct a 3-D volume for each sample. Each volume represents a regular volumetric grid where each voxel has a unique gray-scale value. A dedicated image processing and quantification workflow was applied to calculate the size, morphology, and 3-D distribution of sulfide minerals in the samples using Avizo (FEI) and Matlab codes (Godel, 2013; Godel et al., 2006).

Electron Backscatter Diffraction Analysis

Studied samples are not orientated in the structural framework. Standard uncovered petrographic thin sections were polished mechanically with 1 µm diamond paste, followed by 3 h with 0.06 µm colloidal silica on a Beuhler Vibromet 2 polisher. EBSD analysis was undertaken on a Tescan Mira3 field emission scanning electron microscope (SEM) running Oxford Instruments AZtec acquisition software at Curtin University, Perth (Western Australia). Crystallographic information was collected for six phases (olivine, pargasitic amphibole, enstatite, phlogopite, pyrrhotite, and spinel). Match units used for indexing of these phases are reported in GSA Data Repository Table DR1.[1] Data collection, indexing, and analysis of EBSD patterns were done with AZtecHKL 2.2 acquisition software.

The EBSD maps and pole figures of crystallographic orientation of the main phases were constructed using Oxford Channel 5.12 software. The EBSD data phase maps show the distribution of identified phases based on EBSD data. Maps showing the orientation of the slope of the major axis of the fitted ellipsoid within each grain represent a proxy for shape preferred orientation (SPO). Textural component maps were used to illustrate maximum lattice distortion from a user-selected reference point. All crystallographic data are plotted on a lower-hemisphere, equal-area stereographic projection. Slip system analyses were performed according to methods described in Lloyd and Freeman (1994) and Reddy et al. (2007).

The EBSD olivine phase maps were processed using ImageJ (1.48) software to obtain the slope of the angle of the longest diagonal of the best-fitted ellipsoid, which was later used to characterize the SPO of the olivine crystals. The fabric strength was determined by calculating the *j* index and *M* index of the orientation distribution function (ODF) using the MTex MatLab toolbox (Hielscher and Schaeben, 2008). We calculated the *j* index using the de la Vallée Pousin kernel, with a half-width of 10°, which corresponds to a series expansion of 28. The *j* index has a value of one for a random distribution and a value of infinity for a single crystal (Wenk et al., 1998), and so higher *j* index values indicate stronger fabrics. SPO was tested with the statistical approach proposed by Masuda et al. (1999) and later modified by Piazolo and Passchier (2002). The statistical value *k* is based on common orientation of the long axis of individual grains (for determination of *k*, see Piazolo and Passchier, 2002). We used the classification from Piazolo and Passchier (2002), where SPO categories are represented by: $k \geq 5$ is strong, $2 \leq k \leq 5$ is moderate, and $k < 2$ is low. We applied a Rayleigh test to assess whether there effectively is any statistically significant SPO. Both *k* values and Rayleigh test calculations can be found in the Data Repository material (see footnote 1).

PETROGRAPHY

Sample I2—Core of the Valmaggia Pipe

Sample I2 is a coarse-grained, amphibole-rich, phlogopite-bearing peridotite that exhibits mild brittle deformation, which is reflected by the occurrence of Riedel-like fractures (Figs. 2A and 2C). It contains olivine (~55%), pargasitic amphibole (~25%), orthopyroxene (10%), phlogopite (5%–10%), and sulfide minerals (~1%). Other accessory phases include Cr-spinel and apatite. The rock has a poikilitic texture, which is defined by chadacrystic olivine and oikocrystic orthopyroxene and/or amphibole. Olivine has a subhedral habit and varies in size from ~0.1 to 1 mm

[1]GSA Data Repository Item 2018417, Table DR1: EBSD acquisition parameters and settings; Table DR2: Strength of crystal shape fabric; and Figure DR1: Additional microstructural information on constitute minerals from studied samples, is available at http://www.geosociety.org/datarepository/2018, or on request from editing@geosociety.org.

in diameter (Fig. 2). Olivine grains contain inclusions of Fe-oxides and sulfides. They are pervasively fractured (Fig. 2C and 2F). Brown pleochroic amphibole is generally associated with phlogopite and orthopyroxene, with the latter locally included along the amphibole cleavage planes (Fig. 2F). Large orthopyroxene grains also show evidence of minor alteration (Fig. 2D). Sulfides predominantly occur as pyrrhotite and, to a lesser extent, pentlandite and minor chalcopyrite. In 2-D section, the sulfides occur as small (<150 µm diameter) rounded inclusions within the silicate phases, commonly surrounded by amphibole and/or orthopyroxene. Spinel grains are fine in size (~20 µm in diameter) and are solely observed as inclusions within olivine. Apatite is rare but ubiquitous (<1%) and can form large (~500 µm) crystals commonly associated with phlogopite.

Sample I7—Margin of the Valmaggia Pipe

Sample I7 shows evidence of brittle deformation (Fig. 3). It contains a mineral assemblage similar to the core of the pipe, but it displays a rather different modal abundance of olivine (~65%), pargasitic amphibole (~20%), orthopyroxene (5%), sulfide minerals (5%–10%), and phlogopite (<5%). Similarly, the rock has a poikilitic texture, which is defined by chadacrystic olivine and oikocrystic orthopyroxene and/or amphibole.

Olivine shows significant variance in grain size. The smallest population ranges from ≥100 µm in diameter. The most dominant, midsize grain population is around ~500 µm in diameter, whereas the largest grains can reach up to 2 mm in size (Figs. 3A and 3B). The olivine crystals contain spinel inclusions (Figs. 3C and 3E) and commonly show straight boundaries that meet at equilibrated triple junctions (Figs. 3B, 3C, and 3D). However, where enclosed by sulfide phases, olivine grains are rounded (Fig. 3F). Oikocrystic amphibole records a complex replacement texture with orthopyroxene (Fig. 3C). Orthopyroxene contains numerous fine Fe-oxide inclusions.

The rock texture is characterized by the occurrence of chadacrystic olivine and two oikocryst mineral phases, amphibole and orthopyroxene. Sulfides phases are pyrrhotite, pentlandite, and chalcopyrite. Chalcopyrite occurs as part of large blebs, but it is also locally associated with veins ranging in size from a few micrometers to millimeter size, whereas pyrrhotite and pentlandite are generally present as fine single crystals, or as more composite larger sulfide aggregates (Figs. 3A, 3C, 3E, and 3F). Apatite is rare but pervasive (<1%), and it is commonly spatially associated with Fe-Mn carbonates around the larger sulfide blebs.

3-D DISTRIBUTIONS AND CHARACTERISTICS OF SULFIDE AGGREGATES

Sample I2—Core of the Valmaggia Pipe

Magmatic sulfides in sample I2 represent only 1 vol% of the rock and are finely disseminated within the samples (Fig. 4A). The sulfides are observed within olivine, orthopyroxene, and amphibole, but they are also found at their grain boundaries. The 3-D morphology of the sulfide aggregates with equivalent sphere diameter (ESD) smaller than 100 µm displays little variation (Fig. 4B). These small sulfide aggregates represent ~20 vol% of sulfides (Fig. 4F) and are subspherical in the vast majority of cases (sphericity values > 0.95; Fig. 4G). Conversely, sulfide aggregates with ESD size ranging from 100 to 300 µm exhibit more variable morphologies, from subspherical to slightly elongated aggregates, with aspect ratio up to 3 (Fig. 4C), and with sphericity values varying from 0.75 to 0.92 (Fig. 4G). These sulfides represent ~60 vol% of sulfides.

Magmatic sulfides larger than 300 µm ESD form small interconnected sulfide networks up to 2 mm in Feret's diameter (i.e., the largest intersection in 3-D; Feret's diameter is defined as the distance between the two parallel planes restricting the object perpendicular to that direction) and are located at silicate grain boundaries (Figs. 4D and 4E). These larger sulfides (maximum ESD of 1040 µm) account for ~20 vol% of sulfides. Sulfide aggregate size distribution (CSD) on a plot of ln(PD) (population density) versus ESD size is strongly kinked and can be split into distinctive straight-line segments (Fig. 4H). Sulfide aggregates smaller than 300 µm have a characteristic length of 50 (where characteristic length is given as L_C and corresponds to the mean ESD for a CSD that extends to all aggregate sizes and is defined by −1/slope of the CSD curve), whereas larger sulfide aggregates have a characteristic ESD size of 200 µm (Cashman and Marsh, 1988).

Sample I7—Margin of the Valmaggia Pipe

Magmatic sulfides in sample I7 represent 19 vol% of the rock and exhibit a range of 3-D textures (Fig. 5A). Although sulfides are observed within olivine, orthopyroxene, and amphibole, the vast majority of sulfide is found at grain boundaries. The 3-D morphology of the sulfide aggregates with ESD smaller than 100 µm displays little variation (Fig. 5B). These small sulfide aggregates are subspherical in the vast majority of cases (sphericity values > 0.95; Fig. 5G) and represent <1 vol% of sulfides (Fig. 5F). Sulfide aggregates with ESD size ranging from 100 to 300 µm exhibit more variable morphologies (from subspherical to slightly elongated aggregates with aspect ratio up to 2.5; Fig. 5C), with sphericity values varying from 0.8 to 0.95 (Fig. 5G).

In contrast to sample I2, these sulfides represent ~5.5 vol% of sulfides. Sulfide aggregates with ESD size ranging from 300 to 1000 µm ESD form small interconnected sulfide networks with aggregate sphericity varying from 0.5 to 0.7 (Fig. 5G), and up to 2 mm in Feret's length. These elongated sulfide aggregates are located at silicate grain boundaries (Fig. 5D) and represent ~8 vol% of sulfides (Fig. 5F). Sulfide aggregates larger than 1000 µm ESD account for the vast majority (>80%) of the total sulfide volume (Fig. 5F). These larger sulfide aggregates form complex interconnected 3-D networks (17 observed networks in total) that wet silicate boundaries and extend over 20 mm in Feret's length.

It should be noted that in most cases, the sulfide networks were intersected during sample preparation; hence, the given maximum ESD size is a strict minimum. Sulfide aggregate size distribution (CSD) is displayed on a plot of ln(PD) versus ESD size in Figure 5H. The CSD curve reflects the heterogeneous sulfide distribution at sulfide aggregate sizes greater than 1200 µm ESD. Consequently, the regression curves were only calculated for the smaller size population. The CSD curve for sulfide aggregates smaller than 1200 µm ESD is strongly kinked and can be split into distinct straight-line segments (Fig. 5H, right side). Sulfide aggregates smaller than 300 µm ESD have a characteristic ESD size of 40 µm, whereas larger sulfide aggregates a exhibit characteristic ESD size of 170 µm.

MICROSTRUCTURAL ANALYSIS

Microstructural Characterization of the Core of the Valmaggia Pipe (Sample I2)

The 2-D grain shapes of olivine crystals are mildly elongated; the grain shape map shows two dominant directions in crystal orientation (Fig. 6). One main direction of apparent grain shape orientation is along N-S (yellow and gray-yellow grains), whereas the other is along E-W (blue-gray grains), as shown in Figures 6A and 6C. Olivine grains that are colored in gray are oriented along the NE-SW or NW-SE sample directions (Figs. 6A and 6C). Olivine pole figure data from map 1 show a weak fabric with mild clustering along the {100} and {001} poles, whereas in the case of

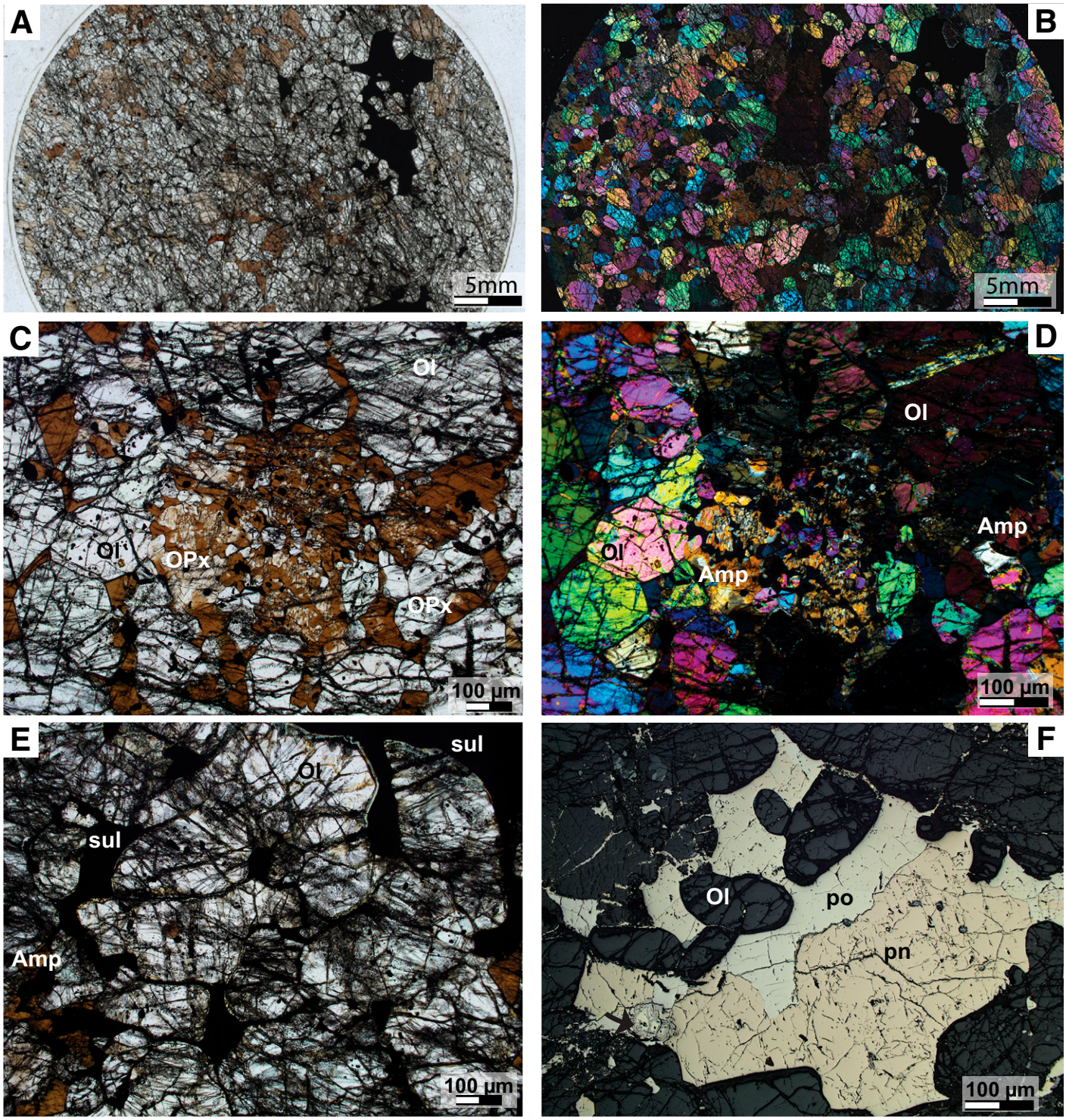

Figure 3. Photomicrographs of I7 (margin of the pipe) Ivrea Verbano sample. (A) Plane-polarized photomicrograph of the 2.5-cm-diameter thin section. (B) Cross-polarized photomicrograph of the 2.5-cm-diameter thin section. (C) Plane-polarized photomicrograph of complex reaction between orthopyroxene and amphibole. (D) Cross-polarized light photomicrograph of the image in C. (E) Plane-polarized light image of fine sulfide crystals (pyrrhotite) enclosed by olivine crystals. (F) Reflected light microphotograph of large sulfide aggregate composed of pyrrhotite and pentlandite. Abbreviations: Ol—olivine; Amp—amphibole; OPx—orthopyroxene; sul—sulphides; po—pyrrhotite; pn—pentlandite.

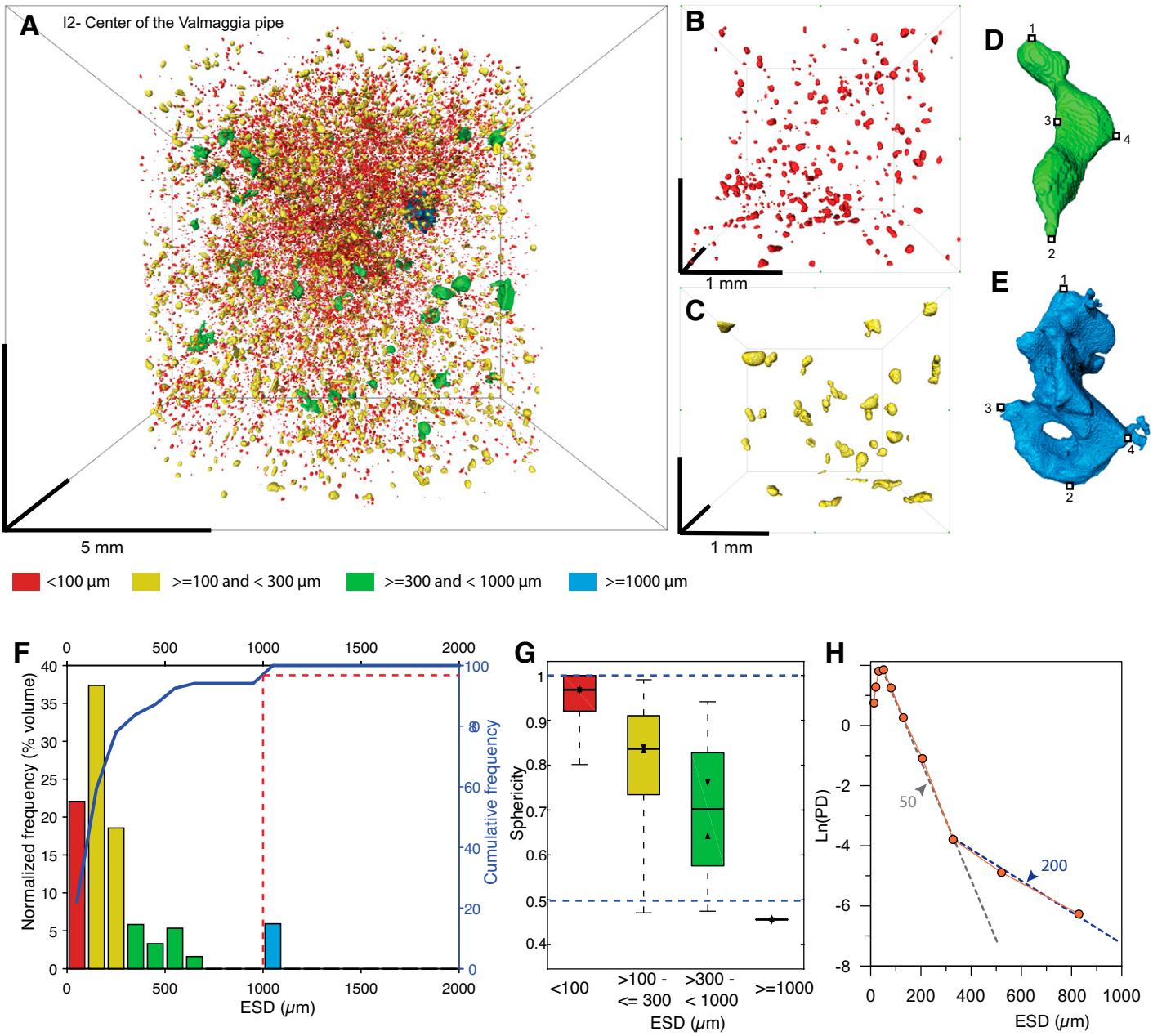

Figure 4. (A) Image of a three-dimensional (3-D) volume of a cylindrical I2 rock sample obtained by high-resolution X-ray computed tomography, and (B–C) 3-D distributions and morphology of the sulfide grains with <100 µm (B), and ≥100–300 µm (C) in diameter. (D–E) 3-D images of common morphology of a sulfide grain with ESD ≥300 and <1000 µm (D) and a sulfide grain with ESD ≥1000 µm (E). (F) Histogram showing size distribution of the sulfide crystals. Blue line represents cumulative frequency. (G) Box-whisker diagram showing sphericity of the sulfide grains according to their grain size. (H) Crystal size distribution curve of the sulfide grains. Blue dotted line represents regression curve. For the steeper regression curve, characteristic aggregate size (Lc) is 50, and for less steep regression curve, Lc is 200. ESD—equivalent sphere diameter.

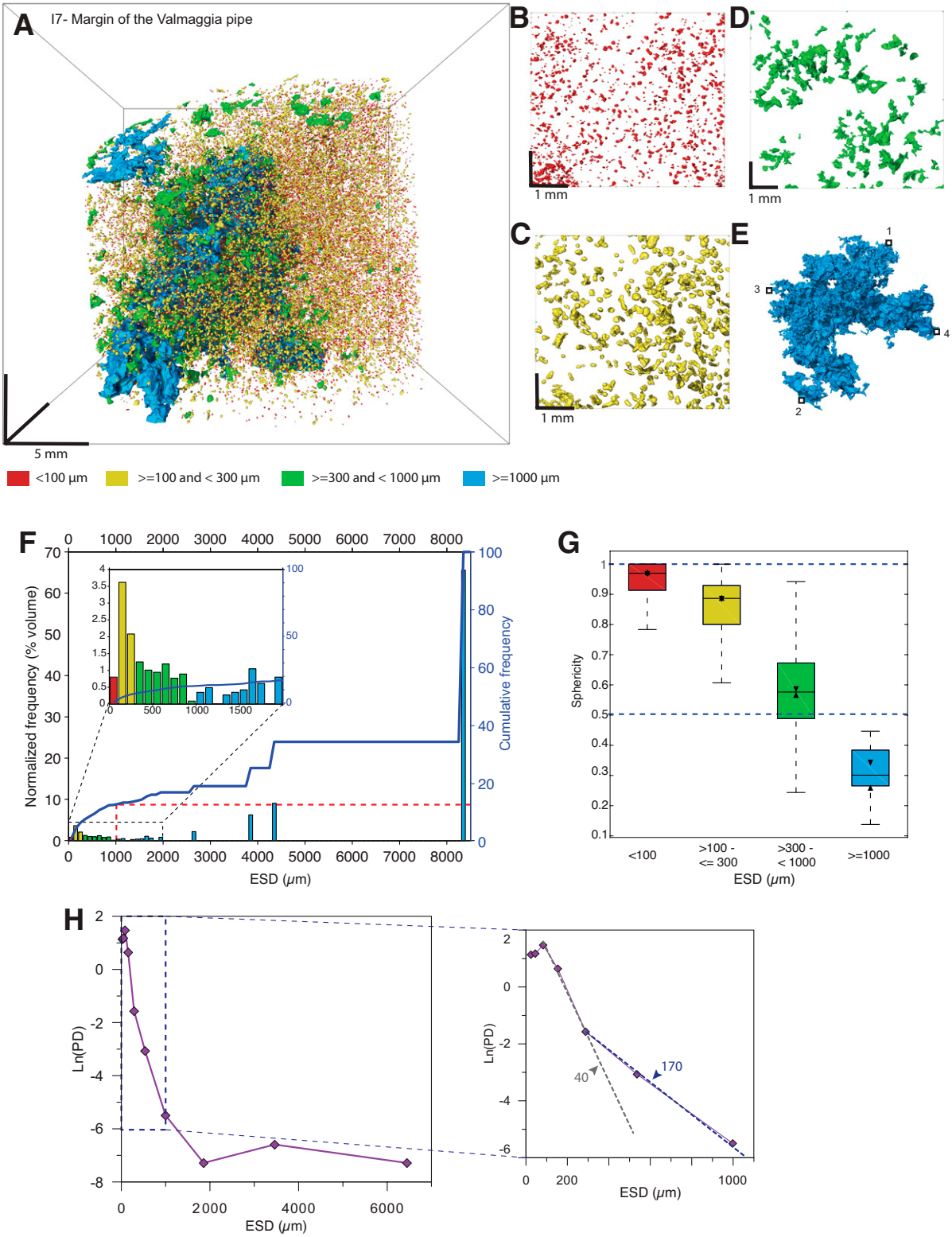

Figure 5. (A) Image of a three-dimensional (3-D) volume of a cylindrical I7 rock sample obtained by high-resolution X-ray computed tomography, and (B–D) 3-D distributions and morphology of the sulfide grains with <100 µm (B), ≥100–300 µm (C), and ≥300 and <1000 µm diameter (D). (E) 3-D image of common morphology of a sulfide grain with ESD ≥1000 µm. (F) Histogram showing size distribution of the sulfide crystals. Blue line represents cumulative frequency. (G) Box-whisker diagram showing sphericity of the sulfide grains according to their grain size. (H) Crystal size distribution curve of the sulfide grains. The zoomed-in diagram of crystal size distribution curve shows distribution of sulfide grains with ≤1000 µm. For the steeper regression curve, characteristic aggregate size (Lc) is 40, and for less steep regression curve, Lc is 170. Blue dotted line represents the regression curve; ESD—equivalent sphere diameter.

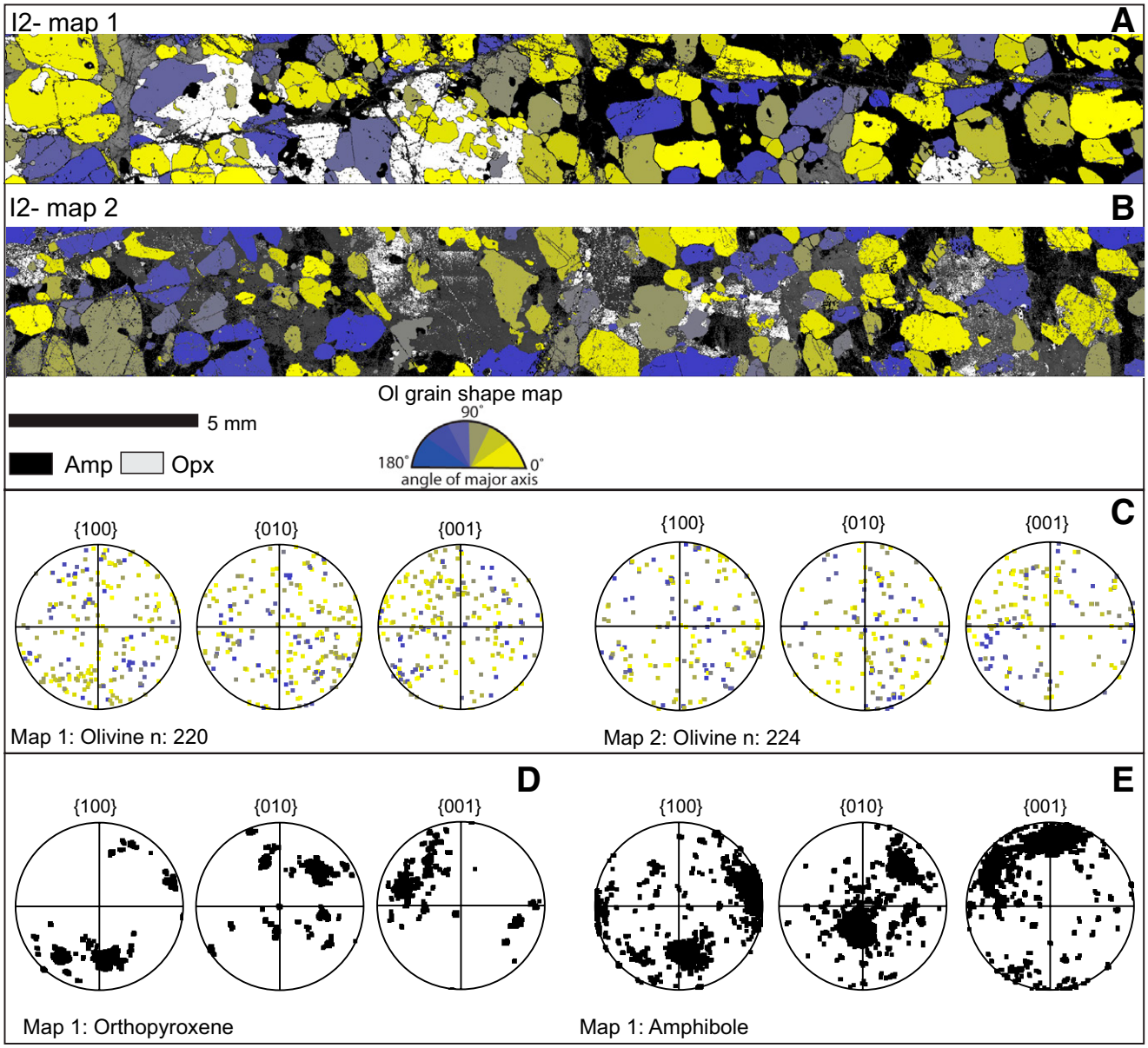

Figure 6. Grain shape olivine maps from I2 sample: (A) map LAM1, and (B) map LAM2. Amphibole (Amp) and orthopyroxene (Opx) are indicated in black and white color, respectively. Grain shape map was constructed based on the long axis of a fitted ellipsoid within each olivine (Ol) crystal. Angle of the long axis varies from 0 to 180° (blue to yellow coloring). (C) Pole figure data for olivine crystals (one point per grain). (D) Pole figure data for orthopyroxene and amphibole. J index—textural index indicating the strength of the fabric.

map 2, data show a weak fabric parallel to the {001} poles (Fig. 6C). The textural indices for maps 1 and 2 are 1.86 and 7.6, respectively.

A statistical test on the presence of SPO gives very low k values (k is based on common orientation of the long axis of individual grains), whereas z values are just above the threshold for the test to be statistically valid (Masuda et al., 1999; Piazolo and Passchier, 2002). Threshold values for z were provided by Piazolo and Passchier (2002), and k and z values from this study are documented in the Data Repository item. Orthopyroxene and amphibole pole figure data show that these two phases have almost identical crystallographic orientation (Figs. 6D and 6E).

Low-angle boundaries in olivine crystals are observed around fine recrystallized grains (Fig. 7; grain 1). The intragrain microstructures of the olivine crystals show a variable degree of lattice distortion (Fig. 7A, grains 1 and 2). Local misorientation within olivine grains varies from low 10° to high 30°. Orientation data of grain 1 show pole figure data that are spread out (Fig. 7B) along dispersion axes (i.e., axes that experienced minimum dispersion; Fig. 7C). Dispersion axes cluster around the (100) and (010) axes (Figs. 7B and 7C). Olivine grains locally show up to 15° of lattice misorientation (Fig. 7A, grain 2), where the low-angle boundary 1 is consistent with formation as a tilt boundary (Fig. 7A, grain 2, boundaries 1 and 2) and deformation by the {010}<100> slip system (Fig. 7D). Low-angle boundary 2 has almost orthogonal orientation with respect to boundary 1. The dispersion axis <010> corresponds well with the misorientation axis, suggesting the {100}<001> slip system (Fig. 7E).

Intragrain microstructure of a small portion of the large oikocrystic amphibole shows lattice distortion of 20° (Fig. 7A, grain 3). The

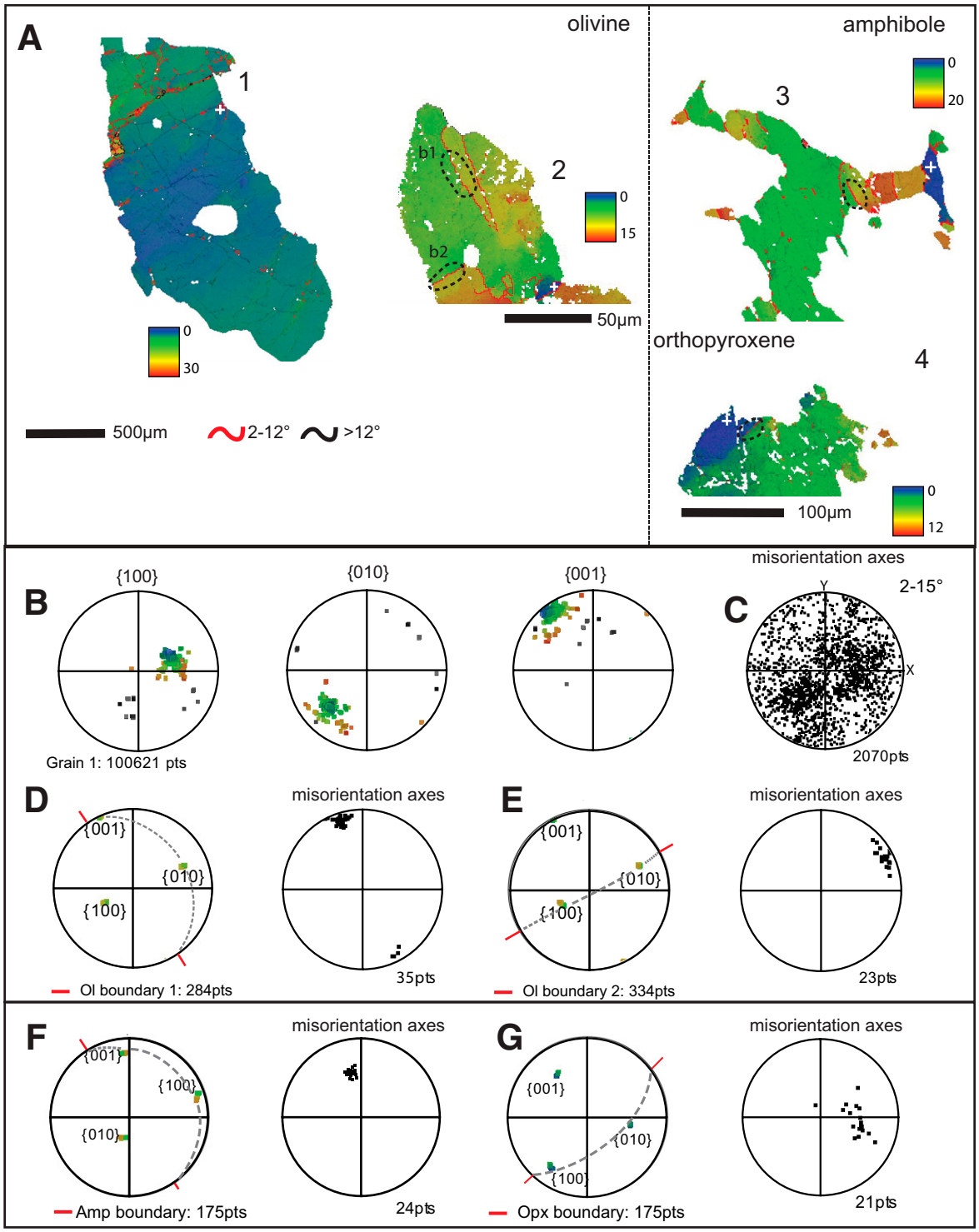

Figure 7. (A) Electron backscatter diffraction (EBSD) data show lattice misorientation within olivine (1–2), amphibole (3), and orthopyroxene (4). Maximum local misorientation from arbitrary point (white cross) varies for each crystal (see respective legend). (B) Pole figure and (C) misorientation axes data from crystal 1. (D–E) Olivine (Ol) low-angle boundary analyses and their respective misorientation axes for boundaries b1 and b2. (F) Amphibole (Amp) low-angle boundary analysis and misorientation axes. (G) Orthopyroxene (Opx) low-angle boundary analysis and misorientation axes.

misorientation axis along the examined low-angle boundary is a result of mixing of (100) and (010) axes (Fig. 7F). However, with the dispersion axis corresponding to <001>, the analyzed boundary is interpreted as a tilt boundary characterized by the {100}<010> slip system (Fig. 7F). Orthopyroxene shows a mild lattice distortion with poorly developed low-angle boundaries (Fig. 7, grain 4). In the case of the examined orthopyroxene low-angle boundary, misorientation axes show mild correlation with dispersion axis (010), suggesting that this is a tilt boundary formed by the operation of the slip system {100}<010> (Fig. 7G).

Microstructural Characterization of the Margin of the Valmaggia Pipe (Sample I7)

The major axis of the fitted ellipsoid of the majority of the fine olivine crystals is oriented NE-SW (blue-gray grains in Fig. 8A). Apparent shape orientation for the larger olivine crystals (>1 mm) is predominantly toward the E-W direction of the sample reference frame (i.e., yellow grains in Fig. 8A). The strength of the olivine fabric is relatively weak, with *j* index of 1.69. There is a mild crystallographic preferred orientation of yellow and blue-gray crystals (smaller fraction and larger E-W–aligned crystals) along {001}, but any apparent SPO of the olivine crystals is not strongly controlled by crystallographic orientation of the same (Fig. 8B). The test on the presence of SPO in the sample gives a very low *k* value but relatively high *z* (see Data Repository Table DR2). Amphibole and orthopyroxene grains show very similar crystallographic orientation (Figs. 8C and 8D). Apart from olivine shape information, the EBSD map also shows a complex relationship between amphibole and orthopyroxene (red rectangle in Fig. 8A).

The large fractured olivine crystal shows large degrees of lattice misorientation of ~30°, whereas the smaller crystal shows relatively mild local misorientation of ~10° (Fig. 9A). Orientation data of the large olivine

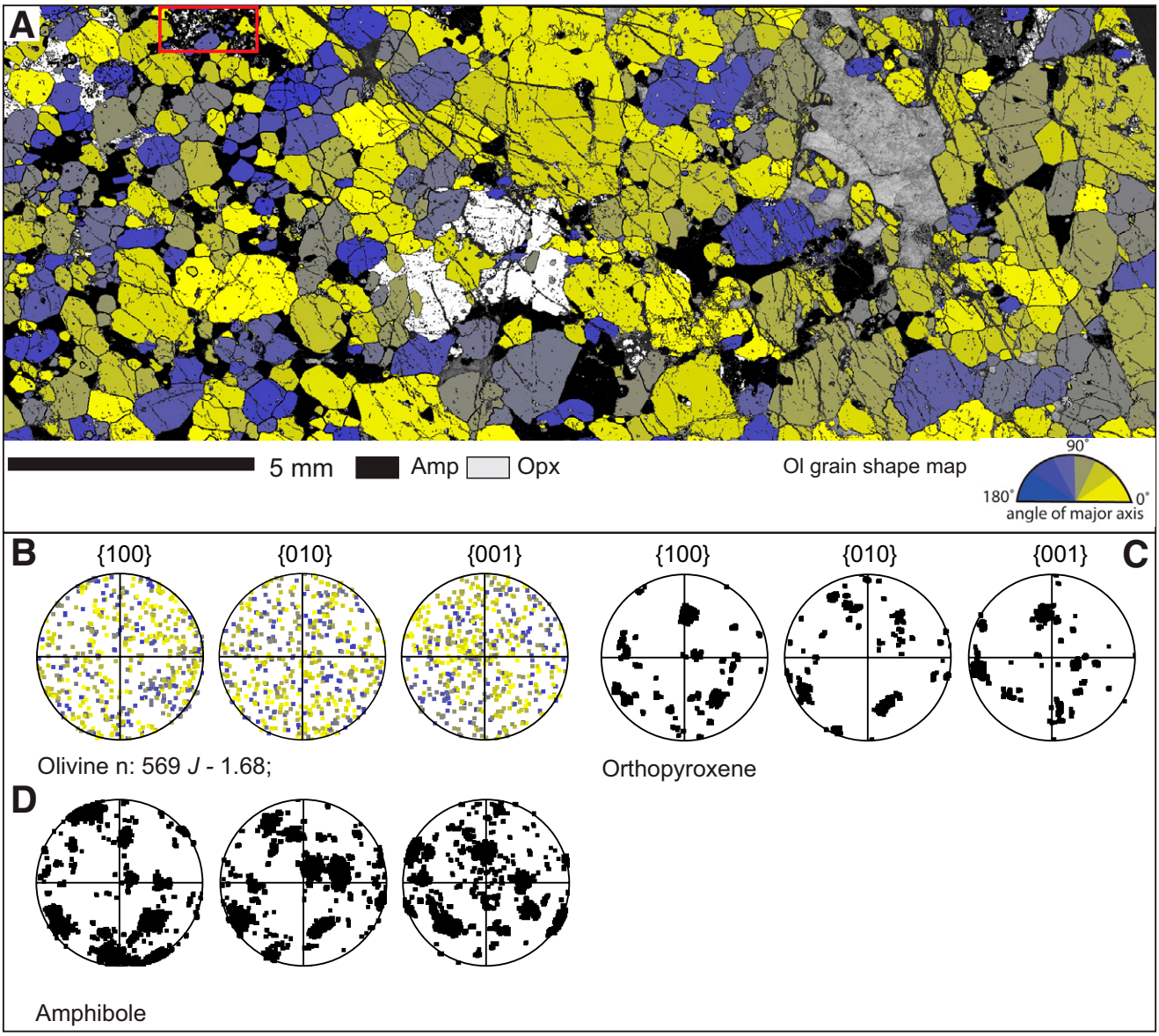

Figure 8. (A) Grain shape olivine maps from I7 sample. Amphibole (Amp) and orthopyroxene (Opx) are indicated in black and white color, respectively. Angle of the long axis varies from 0 to 180° (blue to yellow coloring). (B) Pole figure data for olivine crystals (one point per grain). (C) Pole figure data for orthopyroxene. (D) Pole figure data for amphibole. J index—textural index indicating the strength of the fabric.

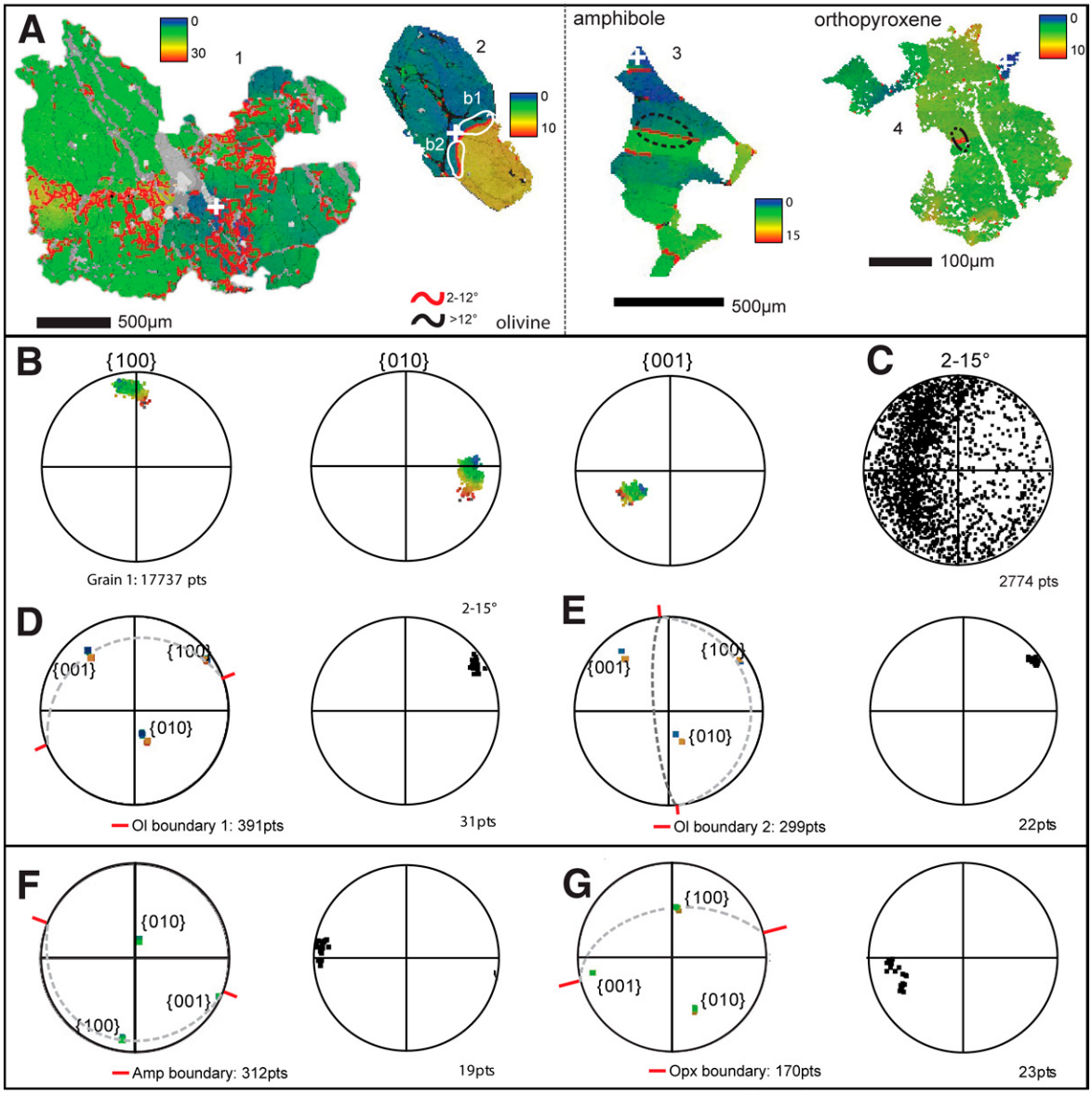

Figure 9. (A) Local misorientation maps for olivine crystal (1 and 2), amphibole (3), and orthopyroxene (4). Maximum local misorientation from arbitrary point (white cross) varies for each crystal (see respective legend). (B) Pole figure and (C) misorientation axes data from olivine crystal 1. (D–E) Olivine (Ol) low-angle boundary pole analyses and their respective misorientation axes for boundaries b1 and b2. (F) Amphibole (Amp) low-angle boundary analysis and corresponding misorientation axes. (G) Orthopyroxene (Opx) low-angle boundary analysis together with misorientation axes.

crystal show significant lattice distortions (Fig. 9B), with orientation of the misorientation axes spread along a great circle (Fig. 9C). On the other hand, the fine olivine grain contains a single curved low-angle boundary (Fig. 9A, grain 2). This boundary was analyzed in two steps: boundary 1 with orientation NE-SW and boundary 2 with orientation of roughly N-S (Fig. 9A, grain 2). The misorientation axis along boundary 1 corresponds to the dispersion axis <100> (Fig. 9D), whereas clustered misorientation axes along boundary 2 correspond to dispersion axis <100> (Fig. 9E). Slip system analyses suggest that boundary 1 corresponds to a tilt boundary characterized by the {001}<010> slip system. The relationship of poles of crystallographic axes and misorientation axes suggest that boundary 2 corresponds to both a twist and tilt type of boundary. Therefore, the slip system cannot be determined with certainty.

Amphibole grains show local lattice distortion of ~10° and contain parallel low-angle boundaries within large single-crystal oikocrysts (Fig. 9A, grain 3). The misorientation axes associated with these low-angle boundaries show a good correlation with the dispersion axis <010> (Fig. 9F). This low-angle boundary corresponds to a tilt boundary associated with the operation of the {010}<100> slip system. Unlike amphiboles, orthopyroxene grains show very mild local distortion (<10°) with weakly developed low-angle boundaries (Fig. 9A, grain 4). Orientation data along the analyzed boundary show minor dispersion of {001}, as shown in Figure 9G. Even though misorientation axes are spread out, they can be weakly correlated with dispersion axis {001} (Fig. 9G). With dispersion axis <001>, the boundary in orthopyroxene can be poorly correlated as a tilt boundary along the {100}<010> slip system.

Microstructural Characterization of the Sulfide Mineralogy of the Valmaggia Pipe

Sulfide grains from the core of the pipe are well rounded and very fine in size (Fig. 10A). These crystals show evidence of mild lattice distortion and contain low-angle boundaries. The pyrrhotite orientation data are random (Fig. 10C), whereas the misorientation axes show a weak griddle distribution (Fig. 10D).

Sulfide grains at the margin of the pipe show a bimodal size distribution (Figs. 3A and 10B). Grains within the sulfide bleb contain numerous low-angle boundaries, with sets of low-angle boundaries that are generally parallel to each other. The orientation data of the pyrrhotite aggregate do not show any strong preferred orientation (Fig. 10D). The same is true for the misorientation axes data (Fig. 10D). Apart from the low-angle boundaries within the aggregate, sulfide grains contain deformation twins. Orientation data of the smaller pyrrhotite grains (<200 µm) show relatively strong crystallographic preferred orientation (CPO) along {0001}, as shown in Figure 10E, whereas their misorientation axes show griddle distribution (Fig. 10E).

Chadacryst-Oikocryst Relationship

We looked in detail at the microstructural relationship between two sets of chadacryst-oikocryst pairs. The emphasis was on documentation of the nature of the misorientation axes within each phase. In the core of the pipe, oikocrysts comprise both orthopyroxene and amphibole; however, the orientation data focus on the relationship between olivine and amphibole (Figs. 11A and 11B). The distributions of average olivine misorientation axes and average orthopyroxene misorientation axes are almost the same (Fig. 11D). In the margin of the pipe (Figs. 11B, 11E, and 11F), the chadacryst-oikocryst pair from the pipe margin comprises numerous olivine crystals that show a random distribution and are surrounded by amphibole (Figs. 11B, 11E, and 11F). The average of amphibole misorientation axes corresponds well with the average of olivine misorientation axes (Figs. 11B, 11E, 11F). The correlation for three subgroups of misorientation axes for olivine and amphibole is shown in Figure 11G.

DISCUSSION

The most important findings from this study provide unique insights into the emplacement dynamics of magmatic conduits, with significant implications for sulfide transport in silicate magmas and associated metal and volatile exchange among different terrestrial reservoirs. Accordingly, the following discussion is focused on three key aspects: (1) segregation and transport of sulfide blebs in hydrous silicate magmas; (2) physical entrainment of dense sulfide blebs during magma flow; and (3) dynamics of hydrous silicate magma emplacement.

Segregation and Transport of Sulfide Blebs in Hydrous Silicate Magmas

The transport of sulfide liquid in silicate magmas is generally considered to be in the form of dispersed immiscible sulfide droplets (Mathez, 1976; Patten et al., 2012; Prichard et al., 2004; Robertson et al., 2015). In cumulate rocks, the behavior of the sulfide liquid mainly depends on the following factors: (1) the topology of the crystal framework (Godel et al., 2006; Rose and Brenan, 2001); (2) the wetting behavior of the sulfide liquid against solid silicate phases (Godel et al., 2006; Barnes et al., 2008); (3) the presence of any trapped silicate liquid (Barnes et al., 2008); and (4) the balance between capillary and gravitational forces (Mungall and Su, 2005; Mungall et al., 2015; Chung and Mungall, 2009).

The proportion, morphology, size, and distribution of sulfide aggregates observed in the rocks can be used to shed light on the processes that led to the transport, segregation, and accumulation of the sulfide liquid (Godel et al., 2006, 2013; Godel, 2015; Robertson et al., 2015). However, most of the existing studies were carried out on relatively dry basalt and komatiite systems erupted at surface or subvolcanic levels. Conversely, the cumulate rocks from the Valmaggia pipe formed from the crystallization of mafic magma with a high volatile content that was emplaced into the lower continental crust (Locmelis et al., 2016; Sessa et al., 2017; Fiorentini et al., 2018).

In the core of the Valmaggia pipe, sulfides represent <2 vol% and are generally small, with ~80 vol% of sulfide represented by subspherical sulfide aggregates smaller than ESD 300 µm. These sulfides are commonly enclosed in olivine, whereas larger sulfide aggregates tend to form small interconnected networks (up to a few millimeters in length) that are surrounded by oikocrysts (amphibole and/or orthopyroxene), as shown in Figure 2F. Conversely, sulfides are larger at the margin of the pipe, where aggregates are characterized by a multimodal sulfide size distribution (Figs. 3 and 5). At the margins, the finer population is similar in shape and size (and composition) to sulfides from the core of the pipe, whereas the coarser sulfide population forms large aggregates and complex interconnected 3-D networks that extend over the length of the samples (Figs. 5 and 10B). These coarse-grained interconnected sulfides wet the surrounding silicate phases (Fig. 5D).

The crystal size distribution curves (CSD) of sulfide aggregates of both the core and margin of the Valmaggia pipe are similar for the sulfide population smaller than 1000 µm ESD (Figs. 4 and 5). The finer sulfide population is texturally similar to that observed in komatiites. This, together with the observation that sulfides are found as inclusions in olivine grains, is interpreted to reflect early saturation of a sulfide liquid, with the consequent homogeneous nucleation of droplets and their entrapment in situ (Godel et al., 2013). This hypothesis is consistent with the intragranular setting of these blebs within silicate phases (Locmelis et al., 2016) and their predominantly mantle sulfur isotope signature (Garuti et al., 2001; Fiorentini et al., 2018).

In contrast, the larger population along the margins of the pipe can be interpreted in three different ways, which are not mutually exclusive.

(1) Based on the observed 3-D morphology and sharp change in the curvature of the CSD curve, the first hypothesis suggests that the largest sulfide blebs (Fig. 5E) formed by coalescence of multiple smaller sulfide droplets; this process could have promoted downward percolation of the sulfides (Godel et al., 2006). The coalescence mechanism would be facilitated if the porosity channels were larger than the coalescing particles (Chung and Mungall, 2009; Barnes et al., 2017). The coalescence could be caused by mechanical instabilities such as small-scale earthquakes, which may have affected the conduit network during emplacement of the magma. It is predicted that coalescence would occur preferentially along the margins of the pipe, as it is likely that these are loci where the crystal mush would experience relatively higher stress regimes than its counterpart in the central portions of the pipe. A localized higher stress regime at the margins of the pipe is supported by the presence of more strongly deformed olivine grains, as well as by evidence of layering due to magmatic flow (Fig. 9A).

(2) In the magmatic literature, a non-coaxial flow occurs whenever there is drag along a boundary surface, where a viscosity contrast exists between two parts of the flow (Paterson et al., 1998). However, due to the enhanced susceptibility of sulfides to subsolidus processes (Vukmanovic, 2014), it would be hard to detect the flow texture of the sulfides from the

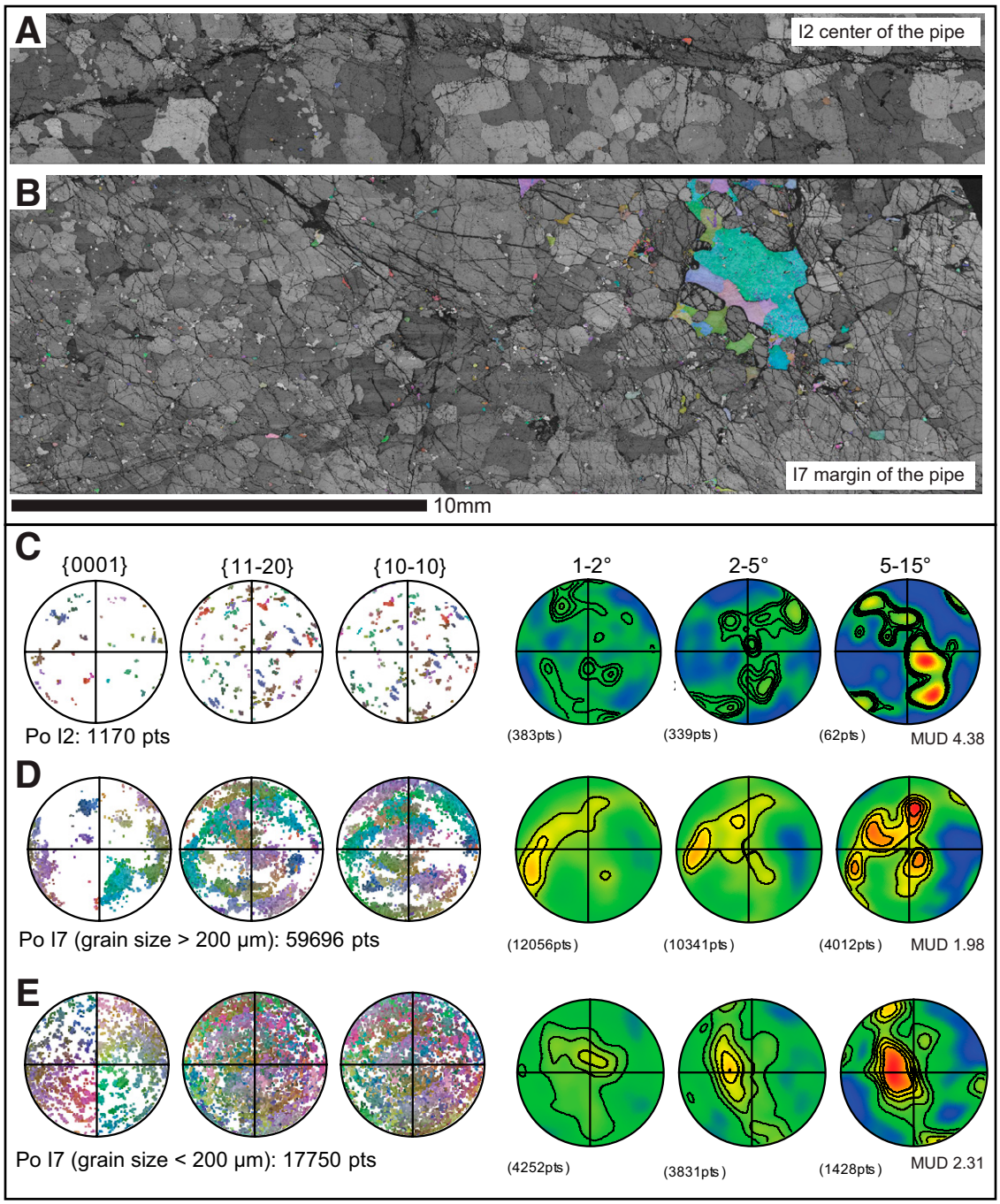

Figure 10. (A–B) Band-contrast, all-Euler orientation maps for pyrrhotite grains of (A) LAM1 (I2 sample) and (B) I7 sample. (C) Pyrrhotite (Po) pole figure data and density contour plot of the misorientation axes. Half width: 20°, cluster size: 10°. (D) Pole figure data of pyrrhotite aggregate and corresponding density contour plot of the misorientation axes. (E) Pole figure data of pyrrhotite grains <200 µm and their corresponding misorientation axes. Half width: 20°, cluster size: 10°.

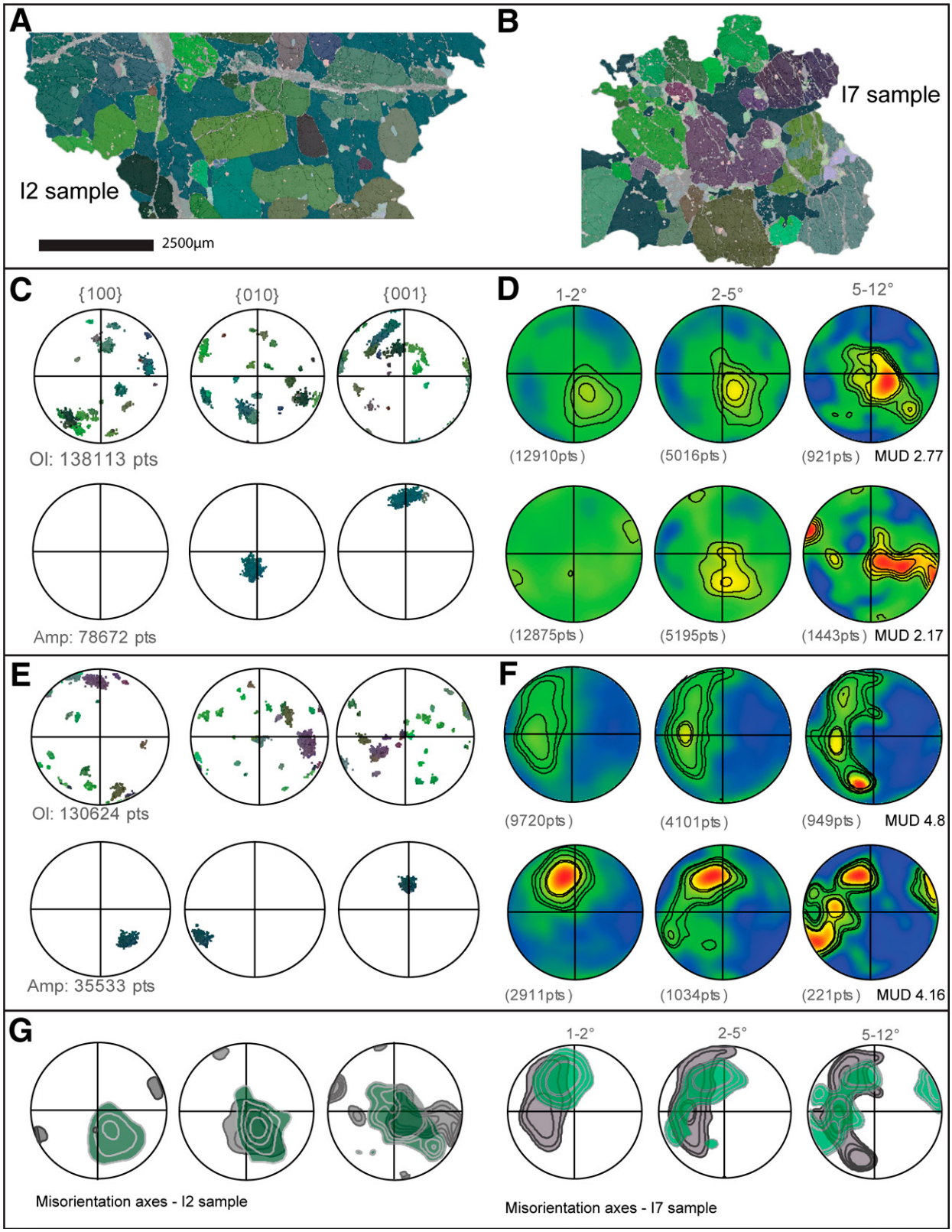

Figure 11. (A) All-Euler orientation map of the olivine-oikocrysts (amphibole) pair from sample I2. (B) All-Euler orientation map of the olivine-oikocrysts (amphibole) pair from sample I7. (C) Pole figure data for olivine (Ol) and amphibole (Amp) from sample I2. (D) Density contour plots of the misorientation axes of corresponding mineral phases from C. (E) Pole figure data for olivine (Ol) and amphibole (Amp) from sample I7. (F) Density contour plots of the misorientation axes of corresponding mineral phases from E. Half width: 20°, cluster size is 10°. (G) Comparison of the misorientation axes density contour plots from olivine-oikocryst pairs.

microstructural record. Nonetheless, it is argued that evidence from sulfide grain-size distribution could be interpreted as reflecting drag along the margin of the pipe, at the contact between the crystal mush hosted in the conduit and the surrounding gabbroic country rocks. Whereas coalescence of sulfide droplets under shear conditions is discarded for dry komatiites (Robertson et al., 2015), more experimental work is required to ascertain whether this mechanism may play a bigger role in volatile-rich melts, such as is the case for the Valmaggia pipe, where the presence of hydrous and carbonated magmatic fluids is postulated (Sessa et al., 2017).

(3) A third hypothesis puts forward the idea that the sulfides were variably transported and deposited according to their wetting behavior in the presence or absence of trapped silicate liquid and/or volatiles (Mungall and Su, 2005; Mungall et al., 2015). This scenario is discussed in the following section.

Physical Entrainment of Dense Sulfide Blebs during Magma Flow

The 3-D HRXCT analyses of sulfides indicate that beside a cotectic-like population of smaller (<1 mm) and rounded intra- and intergranular sulfide blebs, largely made up of pyrrhotite ± pentlandite, the pipe also contains a population of larger intergranular blebs and nodules (5–50 mm in diameter), which are commonly concentrated along the margins of the pipe. These blebs are generally made up of pyrrhotite, with margins comprising an assemblage of pyrrhotite ± pentlandite ± chalcopyrite ± mackinawite ± cubanite and PGE minerals, as discussed in Sessa et al. (2017). The morphology of the larger blebs reveals the presence of embayments and protrusions, in and around which reside a halo of sulfide myrmekites, together with patches of magmatic dolomite and calcite, as well as apatite (Sessa et al., 2017).

An intimate relationship between magmatic sulfides and carbonate phases has recently been observed in the mineralized mafic intrusions that make up the Munali deposit in Zambia (Holwell et al., 2017). At Valmaggia, Sessa et al. (2017) documented in detail the close spatial relationship between carbonates and sulfides, which are intimately associated in nodules up to >1 cm in size. Given the geodynamic setting at the base of the continental crust and the lack of carbonate-bearing phases in the country rocks, Sessa et al. (2017) attributed the presence of carbonate to reflect exsolution of a mantle-derived magmatic carbon-bearing immiscible phase.

Sulfur isotopes indicate that the small blebs (commonly <1 mm, intragranular, and not associated with carbonates) and the larger blebs (centimeter-scale, intergranular, and associated with carbonates) are broadly similar, with mantle-like overlapping $\delta^{34}S$ signatures ranging between 1.03‰ and 1.96‰ (Fiorentini et al., 2018). On the basis of the data and observations from this study, as well as outcomes from previous work at Valmaggia, we put forward the hypothesis that sulfide-saturated magmas derived from a metasomatized mantle source exsolved an immiscible water- and carbon dioxide–bearing phase, which could wet and physically entrain early-formed sulfide blebs. As suggested in the previous section, the coalescence of the sulfide grains preferentially occurred along the margins of the conduits due to higher stress regime. However, the presence of carbonates intimately associated with the larger sulfide nodules implies that volatiles played an active physical role in the entrainment of the dense sulfide liquid.

Dynamics of Hydrous Silicate Magma Emplacement

The EBSD data generated in this study resolve the difference between the microstructural features inherited from the early magmatic history of the Valmaggia pipe and those that reflect the postmagmatic evolution of the IVZ. The Valmaggia pipe contains subrounded olivine crystals, which locally show very mild but distinct SPO. This is interpreted to record evidence of magma flow in the early stages of emplacement of the pipe, when the magma was dynamic and hot (>1000 °C; Locmelis et al., 2016). The data are consistent with geochemical modeling and phase equilibria, which suggest that the pipes represent open-ended conduits for hydrated alkaline mafic magmas within a large magmatic plumbing system (Locmelis et al., 2016). Accordingly, it is proposed that the majority of olivine grains crystallized in situ and were not transported as xenocrysts.

The high modal olivine content that is presently observed in the pipe cannot be reconciled with the dynamics of a flowing mush, as its viscosity would have been too high (Roscoe, 1952; Costa et al., 2009; Cashman et al., 2017). We suggest that the olivine grains that crystallized in situ formed the original crystal framework that filled the pipe conduit, as envisaged by Locmelis et al. (2016) and Sessa et al. (2017). Subsequently, the original olivine-rich cumulate reacted with a volatile-bearing magma, which was mainly channelized along the contacts with the gabbroic country rocks of the mafic complex (Locmelis et al., 2016). This process remobilized the early-formed sulfide blebs into larger nodules, concentrating them along the margins of the pipe.

Even though the ultramafic pipes in the IVZ have been interpreted as only mildly affected by alpine tectonics (Garuti et al., 2001), evidence of microstructural deformation at Valmaggia would suggest that during the tilting and exhumation of the IVZ, the ultramafic pipes recorded both brittle and ductile deformation. More importantly, data show that crystal plasticity in olivine predated brittle deformation (i.e., Riedel-like fractures), which is interpreted to have been associated with the exhumation of the IVZ to middle- and upper-crustal levels during the Jurassic, thrusting and erosion in the Eocene, and final exhumation in the Miocene (Siegesmund et al., 2008; Wolff et al., 2012).

The crystallographic similarity of amphibole and orthopyroxene suggests that the former resulted from a hydration reaction of orthopyroxene. Such a crystallographic relationship has previously been described in McNamara et al. (2012), where retrograde barroisite replaced omphacite while keeping the same crystal orientation (i.e., mimetic growth). Both amphibole and orthopyroxene show a similar deformation microstructure, suggesting that this reaction occurred early (Figs. 6D, 6E, and 7A; see also Data Repository Item). If amphibole were the product of later fluid activity associated with postmagmatic processes, amphibole would either record a different deformation microstructure, or it would be entirely undeformed, which is not the case. Hence, it is likely that the reaction from orthopyroxene to amphibole reflects a magmatic process, thus supporting the model of Locmelis et al. (2016) and Sessa et al. (2017).

The observed slip systems in the olivine crystals from the core of the pipe (sample I2) correspond to a moderate stress regime (E slip system), whereas the olivine grains from the pipe margin (sample I7) do not correspond to any of the slips systems defined by Karato and Wu (1993) or Katayama et al. (2004). Therefore, to better understand the deformation history of these rocks, it is important to constrain the relationship between the chadacryst-oikocryst pairs. In both the central and marginal samples of the pipe, the misorientation axes within olivine crystals and their surrounding oikocrysts show a systematic relationship with their crystallographic orientation. In the core of the pipe, the misorientation axes of both olivine and amphibole are remarkably similar (sample I2; Fig. 11G), while good correlation also occurs between olivine and amphibole misorientation axes along the margins of the pipe (sample I7; Fig. 11G).

Investigation of the intragrain misorientation axes, which are responsible for the dispersion of crystallographic axes, and of the mean orientations of low-angle misorientation axes can be used to constrain the orientation of macroscopic kinematic misorientation axes (Michels et al., 2015;

Reddy and Buchan, 2005). However, with the limited number of samples available in this study, it is hard to extract the kinematic data. In the case of multiple deformation events imposed on the rock, the orientation of the misorientation axes in constitutive phases can become highly complex. As an example, Kaczmarek et al. (2011) observed such a scenario within zircon grains from the Lanzo Massif, western Alps, where the lack of systematic alignment of misorientation axes led to the interpretation that the initial geometry of the misorientation axes had been modified by rigid grain misorientation.

With our data set, due to the similarity in orientations of the misorientation axes for olivine, orthopyroxene, and amphibole (Fig. 11; see Data Repository Item for orthopyroxene data), it is safe to conclude that the Valmaggia pipe experienced one main deformation event that simultaneously deformed olivine and orthopyroxene. The slight discrepancy with the misorientation axis of amphibole (Fig. 11G) likely reflects its later appearance. During the evolution of the magmatic plumbing network where the pipe developed, the stress field may have changed between the emplacement of the silicate melt and subsequent hydration (Locmelis et al., 2016; Sessa et al., 2017). The main silicate phases would otherwise display a more complex deformation pattern, which would have been acquired during the emplacement of the magma. The mild apparent SPO suggests that only a small fraction of the olivine that crystallized was affected by magma flow during emplacement along the conduits, whereas the majority of olivine grains crystallized upon emplacement (i.e., olivine grains are not mantle xenoliths). This interpretation agrees with the relatively low forsterite content of the olivine grains from the Valmaggia pipe (Fiorentini et al., 2002).

CONCLUSIONS

This study provides new data that help to unravel the emplacement dynamics of magmatic pipe conduits in the deep continental crust. As a natural laboratory, we focused on the Valmaggia pipe in the Ivrea-Verbano Zone of Italy. The pipe comprises a volatile-rich peridotite, which contains disseminated, blebby, and semimassive sulfides enriched in nickel, copper, and PGEs. Olivine crystals from the pipe show evidence of mild but detectable SPO, implying that flow texture was recorded during the early (>1000 °C) stages of magma emplacement. The shape and texture of the intragranular sulfide blebs are in agreement with isotopic information, supporting a mantle-derived origin for sulfur. The observed sulfide size distribution between the central and marginal areas of the Valmaggia pipe is principally due to the dynamics of the magma upon emplacement, and may locally record the role of water- and carbon dioxide–bearing volatiles in the physical entrainment of dense sulfide liquids.

In this context, the larger sulfide aggregates forming the bulk of the Ni-Cu-PGE sulfide mineralization along the margins of the Valmaggia pipe can be interpreted in different ways that are not mutually exclusive: (1) They formed by coalescence of a large number of the smaller sulfide droplets, where the coalescence was triggered by instabilities; (2) they formed as a result of different wetting behavior in the presence of silicate liquid and/or volatile; and/or (3) they formed by drag friction during the ascent of the silicate magma transporting its sulfide cargo. Outcomes from this study demonstrate the power of integration of electron backscatter diffraction and three-dimensional high-resolution X-ray computed tomography analyses on spatially constrained samples in unraveling emplacement dynamics of magmas emplaced in the deep continental crust.

ACKNOWLEDGMENTS

We thank Federica Zaccarini and Giorgio Garuti for sharing with us their incredible knowledge of the Ivrea-Verbano Zone, for guidance during field work, and for the numerous constructive discussions on the genesis of the pipes. Nick Arndt, Carole Cordier, Steve Barnes, Marilena Moroni, and Stefano Caruso are thanked for insightful discussions and logistical support in the field. We thank Laurent Godin for his editorial work. Nick Arndt and another anonymous reviewer are acknowledged for their constructive criticism. Vukmanovic was supported by a Marie Curie Individual Fellowship. Fiorentini and Reddy acknowledge support through the Australian Research Council (ARC) Centre of Excellence for Core to Crust Fluid Systems (CE11E0070). Fiorentini acknowledges support from the Australian Research Council through Linkage Project LP120100668 and the Future Fellowship Scheme (FT110100241). This is contribution 1214 from the ARC Centre of Excellence for Core to Crust Fluid Systems (http://www.ccfs.mq.edu.au).

REFERENCES CITED

Barnes, S.J., Fiorentini, M.L., Austin, P., Gessner, K., Hough, R., and Squelch, A., 2008, Three-dimensional morphology of magmatic sulfides sheds light on ore formation and sulfide melt migration: Geology, v. 36, p. 655–658, https://doi.org/10.1130/G24779A.1.

Barnes, S.J., Cruden, A.R., Arndt, N., and Saumur, B.M., 2016, The mineral system approach applied to magmatic Ni-Cu-PGE sulphide deposits: Ore Geology Reviews, v. 76, p. 296–316, https://doi.org/10.1016/j.oregeorev.2015.06.012.

Barnes, S.J., Mungall, J.E., Le Vaillant, M., Godel, B., Lesher, C.M., Holwell, D., Lightfoot, P.C., Krivolutskaya, N., and Wei, B., 2017, Sulfide-silicate textures in magmatic Ni-Cu-PGE sulfide ore deposits: Disseminated and net-textured ores: The American Mineralogist, v. 102, p. 473–506, https://doi.org/10.2138/am-2017-5754.

Bea, F., and Montero, P., 1999, Behavior of accessory phases and redistribution of Zr, REE, Y, Th, and U during metamorphism and partial melting of metapelites in the lower crust: An example from the Kinzigite Formation of Ivrea-Verbano, NW Italy: Geochimica et Cosmochimica Acta, v. 63, p. 1133–1153, https://doi.org/10.1016/S0016-7037(98)00292-0.

Boriani, A., Origoni, E.G., Borghi, A., and Caironi, V., 1990, The evolution of the "Serie dei Laghi" (Strona-Ceneri and Scisti dei Laghi): The upper component of the Ivrea-Verbano crustal section, southern Alps, north Italy and Ticino, Switzerland: Tectonophysics, v. 182, p. 103–118, https://doi.org/10.1016/0040-1951(90)90345-9.

Cashman, K.V., and Marsh, B.D., 1988, Crystal size distribution (CSD) in rocks and the kinetics and dynamics of crystallization II: Makaopuhi lava lake: Contributions to Mineralogy and Petrology, v. 99, p. 292–305, https://doi.org/10.1007/BF00375363.

Cashman, K.V., Sparks, R.S.J., and Blundy, J.D., 2017, Vertically extensive and unstable magmatic systems: A unified view of igneous processes: Science, v. 355, https://doi.org/10.1126/science.aag3055.

Chung, H.-Y., and Mungall, J.E., 2009, Physical constraints on the migration of immiscible fluids through partially molten silicates, with special reference to magmatic sulfide ores: Earth and Planetary Science Letters, v. 286, p. 14–22, https://doi.org/10.1016/j.epsl.2009.05.041.

Costa, A., Caricchi, L., and Bagdassarov, N., 2009, A model for the rheology of particle-bearing suspensions and partially molten rocks: Geochemistry Geophysics Geosystems, v. 10, Q03010, https://doi.org/10.1029/2008GC002138.

Ferrario, A., Garuti, G., and Sighinolfi, G.P., 1982, Platinum and palladium in the Ivrea-Verbano basic complex, western Alps, Italy: Economic Geology, v. 77, p. 1548–1555, https://doi.org/10.2113/gsecongeo.77.6.1548.

Fiorentini, M.L., Grieco, G., Ferrario, A., and Tunesi, A., 2002, Petrological and metallogenic outlines of the Valmaggia ultramafic pipe (Ivrea Zone), NW Alps, Italy: Periodico di Mineralogia, v. 71, p. 219–239.

Fiorentini, M.L., Beresford, S.W., and Barley, M.E., 2008, Ruthenium-chromium variation: A new lithogeochemical tool in the exploration for komatiite-hosted Ni-Cu-(PGE) deposits: Economic Geology, v. 103, p. 431–437.

Fiorentini, M.L., LaFlamme, C., Denyszyn, S., Mole, D., Maas, R., Locmelis, M., Caruso, S., and Bui, T.H., 2018, Post-collisional alkaline magmatism as gateway for metal and sulfur enrichment of the continental lower crust: Geochimica et Cosmochimica Acta, v. 223, p. 175–197, https://doi.org/10.1016/j.gca.2017.11.009.

Garuti, G., Rivalenti, G., Rossi, A., Siena, F., and Sinigoi, S., 1980, The Ivrea-Verbano mafic ultramafic complex of the Italian western Alps: Discussion of some petrologic problems and a summary: Rendiconti della Società Italiana di Mineralogia e Petrologia, v. 36, p. 717–749.

Garuti, G., Fiandri, P., and Rossi, A., 1986, Sulfide composition and phase relations in the Fe-Ni-Cu ore deposits of the Ivrea-Verbano basic complex (western Alps, Italy): Mineralium Deposita, v. 21, p. 22–34, https://doi.org/10.1007/BF00204358.

Garuti, G., Bea, F., Zaccarini, F., and Montero, P., 2001, Age, geochemistry and petrogenesis of the ultramafic pipes in the Ivrea Zone, NW Italy: Journal of Petrology, v. 42, p. 433–457, https://doi.org/10.1093/petrology/42.2.433.

Godel, B., 2013, High-resolution X-ray computed tomography and its application to ore deposits: From data acquisition to quantitative three-dimensional measurements with case studies from Ni-Cu-PGE deposits: Economic Geology, v. 108, p. 2005–2019, https://doi.org/10.2113/econgeo.108.8.2005.

Godel, B., 2015, Platinum-group element deposits in layered intrusions: Recent advances in the understanding of the ore forming processes, *in* Charlier, B., ed., Layered Intrusions: Dordrecht: Springer, p. 379–432, https://doi.org/10.1007/978-94-017-9652-1_9.

Godel, B., Barnes, S.J., and Maier, W.D., 2006, 3-D distribution of sulphide minerals in the Merensky Reef (Bushveld Complex, South Africa) and the J-M Reef (Stillwater Complex, USA) and their relationship to microstructures using X-ray computed tomography: Journal of Petrology, v. 47, p. 1853–1872, https://doi.org/10.1093/petrology/egl029.

Godel, B., Barnes, S.J., and Barnes, S.-J., 2013, Deposition mechanisms of magmatic sulphide liquids: Evidence from high-resolution X-ray computed tomography and trace element chemistry of komatiite-hosted disseminated sulphides: Journal of Petrology, v. 54, p. 1455–1481, https://doi.org/10.1093/petrology/egt018.

Guergouz, C., Martin, L., Vanderhaeghe, O., Thébaud, N., and Fiorentini, M., 2018, Zircon and monazite petrology record of prolonged amphibolite to granulite facies metamorphism in

the Ivrea-Verbano and Strona-Ceneri zones, NW Italy: Lithos, v. 308–309, p. 1–18, https://doi.org/10.1016/j.lithos.2018.02.014.

Hartmann, G., and Wedepohl, K.H., 1993, The composition of peridotite tectonites from the Ivrea complex, northern Italy: Residues from melt extraction: Geochimica et Cosmochimica Acta, v. 57, p. 1761–1782, https://doi.org/10.1016/0016-7037(93)90112-A.

Hielscher, R., and Schaeben, H., 2008, A novel pole figure inversion method: Specification of the MTEX algorithm: Journal of Applied Crystallography, v. 41, p. 1024–1037, https://doi.org/10.1107/S0021889808030112.

Holwell, D.A., Mitchell, C.L., Howe, G.A., Evans, D.M., Ward, L.A., and Friedman, R., 2017, The Munali Ni sulfide deposit, southern Zambia: A multi-stage, mafic-ultramafic, magmatic sulfide-magnetite-apatite-carbonate megabreccia: Ore Geology Reviews, v. 90, p. 553–575, https://doi.org/10.1016/j.oregeorev.2017.02.034.

Kaczmarek, M.-A., Reddy, S.M., and Timms, N.E., 2011, Evolution of zircon deformation mechanisms in a shear zone (Lanzo massif, western Alps): Lithos, v. 127, p. 414–426, https://doi.org/10.1016/j.lithos.2011.09.016.

Karato, S.-I., and Wu, P., 1993, Rheology of the upper mantle—A synthesis: Science, v. 260, p. 771–778, https://doi.org/10.1126/science.260.5109.771.

Katayama, I., Jung, H., and Karato, S., 2004, New type of olivine fabric from deformation experiments at modest water content and low stress: Geology, v. 32, p. 1045–1048, https://doi.org/10.1130/G20805.1.

Lloyd, G.E., and Freeman, B., 1994, Dynamic recrystallization of quartz under greenschist conditions: Journal of Structural Geology, v. 16, p. 867–881, https://doi.org/10.1016/0191-8141(94)90151-1.

Locmelis, M., Fiorentini, M.L., Rushmer, T., Arevalo, R., Adam, J., and Denyszyn, S.W., 2016, Sulfur and metal fertilization of the lower continental crust: Lithos, v. 244, p. 74–93, https://doi.org/10.1016/j.lithos.2015.11.028.

Masuda, T., Kugimiya, Y., Aoshima, I., Hara, Y., and Ikei, H., 1999, A statistical approach to determination of a mineral lineation: Journal of Structural Geology, v. 21, p. 467–472, https://doi.org/10.1016/S0191-8141(99)00005-X.

Mathez, E.A., 1976, Sulfur solubility and magmatic sulfides in submarine basalt glass: Journal of Geophysical Research, v. 81, p. 4269–4276, https://doi.org/10.1029/JB081i023p04269.

McNamara, D.D., Wheeler, J., Pearce, M., and Prior, D.J., 2012, Fabrics produced mimetically during static metamorphism in retrogressed eclogites from the Zermatt-Saas Zone, western Italian Alps: Journal of Structural Geology, v. 44, p. 167–178, https://doi.org/10.1016/j.jsg.2012.08.006.

Mehnert, K.R., 1975, The Ivrea Zone, a model of the deep crust: Neues Jahrbuch für Mineralogie, Abhandlungen, v. 125, p. 156–199.

Michels, Z.D., Tikoff, B., Kruckenberg, S.C., and Davis, J.R., 2015, Determining vorticity axes from grain-scale dispersion of crystallographic orientations: Geology, v. 43, p. 803–806, https://doi.org/10.1130/G36868.1.

Mungall, J.E., and Su, S., 2005, Interfacial tension between magmatic sulfide and silicate liquids: Constraints on the kinetics of sulfide liquation and sulfide migration through silicate rocks: Earth and Planetary Science Letters, v. 234, p. 135–149, https://doi.org/10.1016/j.epsl.2005.02.035.

Mungall, J.E., Brenan, J.M., Godel, B., Barnes, S.J., and Gaillard, F., 2015, Transport of metals and sulphur in magmas by flotation of sulphide melt on vapour bubbles: Nature Geoscience, v. 8, p. 216–219, https://doi.org/10.1038/ngeo2373.

Paterson, S.R., Fowler, T.K., Jr., Schmidt, K.L., Yoshinobu, A.S., Yuan, E.S., and Miller, R.B., 1998, Interpreting magmatic fabric patterns in plutons: Lithos, v. 44, p. 53–82.

Patten, C., Barnes, S.J., and Mathez, E.A., 2012, Textural variations in MORB sulfide droplets due to differences in crystallization history: Canadian Mineralogist, v. 50, p. 675–692, https://doi.org/10.3749/canmin.50.3.675.

Peressini, G., Quick, J.E., Sinigoi, S., Hofmann, A.W., and Fanning, M., 2007, Duration of a large mafic intrusion and heat transfer in the lower crust: A SHRIMP U-Pb zircon study in the Ivrea-Verbano Zone (western Alps, Italy): Journal of Petrology, v. 48, p. 1185–1218, https://doi.org/10.1093/petrology/egm014.

Piazolo, S., and Passchier, C.W., 2002, Controls on lineation development in low to medium grade shear zones: A study from the Cap de Creus Peninsula, NE Spain: Journal of Structural Geology, v. 24, p. 25–44, https://doi.org/10.1016/S0191-8141(01)00045-1.

Pin, C., and Sills, J.D., 1986, Petrogenesis of layered gabbros and ultramafic rocks from Val Sesia, the Ivrea Zone, NW Italy: Trace element and isotope geochemistry, *in* Dawson, J.B., Carswell, D.A., Hall, J., and Wedepohl, K.H., eds., The Nature of the Lower Continental Crust: Geological Society, London, Special Publication 24, p. 231–249, https://doi.org/10.1144/GSL.SP.1986.024.01.21.

Prichard, H.M., Hutchinson, D., and Fisher, P.C., 2004, Petrology and crystallization history of multiphase sulfide droplets in a mafic dike from Uruguay: Implications for the origin of Cu-Ni-PGE sulfide deposits: Economic Geology, v. 99, p. 365–376, https://doi.org/10.2113/gsecongeo.99.2.365.

Quick, J.E., Sinigoi, S., Mayer, A., Quick, J.E., Clemens-Knott, D., Mayer, A., Demarchi, G., Mazzucchelli, M., Negrini, L., and Rivalenti, G., 1994, Emplacement dynamics of a large mafic intrusion in the lower crust, Ivrea-Verbano Zone, northern Italy: Journal of Geophysical Research–Solid Earth (1978–2012), v. 99, p. 21,559–21,573.

Quick, J.E., Sinigoi, S., Snoke, A.W., Kalakay, T.J., Mayer, A., and Peressini, G., 2002, Geologic map of the southern Ivrea-Verbano Zone, northwestern Italy: US Geological Survey IMAP 2776, scale 1:25,000, https://doi.org/10.3133/i2776.

Reddy, S.M., and Buchan, C., 2005, Constraining kinematic rotation axes in high-strain zones: A potential microstructural method?, *in* Gapais, D., Brun, J.P., and Cobbold, P.R., eds., Deformation Mechanisms, Rheology and Tectonics: From Minerals to the Lithosphere: Geological Society, London, Special Publication 243, p. 1–10, https://doi.org/10.1144/GSL.SP.2005.243.01.02.

Reddy, S.M., Timms, N.E., Pantleon, W., Trimby, P., and Trimby, T., 2007, Quantitative characterization of plastic deformation of zircon and geological implications: Contributions to Mineralogy and Petrology, v. 153, p. 625–645, https://doi.org/10.1007/s00410-006-0174-4.

Rivalenti, G., Rossi, A., Siena, F., and Sinigoi, S., 1984, The layered series of the Ivrea-Verbano igneous complex, western Alps, Italy: Tschermak's Mineralogische und Petrographische Mitteilungen, v. 33, p. 77–99, https://doi.org/10.1007/BF01083065.

Robertson, J.C., Barnes, S.J., and Le Vaillant, M., 2015, Dynamics of magmatic sulphide droplets during transport in silicate melts and implications for magmatic sulphide ore formation: Journal of Petrology, v. 56, p. 2445–2472, https://doi.org/10.1093/petrology/egv078.

Roscoe, R., 1952, The viscosity of suspensions of rigid spheres: British Journal of Applied Physics, v. 3, p. 267, https://doi.org/10.1088/0508-3443/3/8/306.

Rose, L.A. and Brenan, J.M., 2001, Wetting properties of Fe-Ni-Co-Cu-OS melts against olivine: Implications for sulfide melt mobility: Economic Geology, v. 96, p. 145–157.

Rutter, E.H., Brodie, K.H., and Evans, P.J., 1993, Structural geometry, lower crustal magmatic underplating and lithospheric stretching in the Ivrea-Verbano Zone, northern Italy: Journal of Structural Geology, v. 15, p. 647–662, https://doi.org/10.1016/0191-8141(93)90153-2.

Schmid, S.M., Zingg, A., and Handy, M., 1987, The kinematics of movements along the Insubric Line and the emplacement of the Ivrea Zone: Tectonophysics, v. 135, p. 47–66, https://doi.org/10.1016/0040-1951(87)90151-X.

Schnetger, B., 1994, Partial melting during the evolution of the amphibolite- to granulite-facies gneisses of the Ivrea Zone, northern Italy: Chemical Geology, v. 113, p. 71–101, https://doi.org/10.1016/0009-2541(94)90006-X.

Sessa, G., Moroni, M., Tumiati, S., Caruso, S., and Fiorentini, M.L., 2017, Ni-Fe-Cu-PGE ore deposition driven by metasomatic fluids and melt-rock reactions in the deep crust: The ultramafic pipe of Valmaggia, Ivrea-Verbano, Italy: Ore Geology Reviews, v. 90, p. 485–509, https://doi.org/10.1016/j.oregeorev.2017.05.028.

Shervais, J.W., and Mukasa, S.B., 1991, The Balmuccia orogenic lherzolite massif, Italy: Journal of Petrology, Special Volume 2, p. 155–174, https://doi.org/10.1093/petrology/Special_Volume.2.155.

Siegesmund, S., Layer, P., Dunkl, I., Vollbrecht, A., Steenken, A., Wemmer, K., and Ahrendt, H., 2008, Exhumation and deformation history of the lower crustal section of the Valstrona di Omegna in the Ivrea Zone, southern Alps, *in* Siegesmund, S., Fügenschuh, B., and Froitzheim, N., eds., Tectonic Aspects of the Alpine-Dinaride-Carpathian System: Geological Society, London, Special Publication 298, p. 45–68, https://doi.org/10.1144/SP298.3.

Vukmanovic, Z., 2014, Microstrucutral Characteristaion of Sulphide and Oxide Minerals in Magmatic Suphide Ores [Ph.D. thesis]: Perth, Australia, University of Western Australia, 201 p.

Wenk, H.R., Matthies, S., Donovan, J., and Chateigner, D., 1998, BEARTEX: A Windows-based program system for quantitative texture analysis: Journal of Applied Crystallography, v. 31, p. 262–269, https://doi.org/10.1107/S002188989700811X.

Wolff, R., Dunkl, I., Kiesselbach, G., Wemmer, K., and Siegesmund, S., 2012, Thermochronological constraints on the multiphase exhumation history of the Ivrea-Verbano Zone of the southern Alps: Tectonophysics, v. 579, p. 104–117, https://doi.org/10.1016/j.tecto.2012.03.019.

Zaccarini, F., Garuti, G., Fiorentini, M.L., Locmelis, M., Kollegger, P., and Thalhammer, O.A.R., 2014, Mineralogical hosts of platinum group elements (PGE) and rhenium in the magmatic Ni-Fe-Cu sulfide deposits of the Ivrea Verbano Zone (Italy): An electron microprobe study: Neues Jahrbuch für Mineralogie, Abhandlungen, v. 191, p. 169–187, https://doi.org/10.1127/0077-7757/2014/0255.

MANUSCRIPT RECEIVED 16 MARCH 2018
REVISED MANUSCRIPT RECEIVED 12 SEPTEMBER 2018
MANUSCRIPT ACCEPTED 30 OCTOBER 2018